Analysis of EMCCD Gain Estimation Techniques for use in Astronomical Instruments

Thesis by
Donal McErlean

In Partial Fulfillment of the Requirements for the
Degree of
Master of Science in Applied Physics

Under the supervision
of Dr Nicholas Devaney

School of Natural Sciences
Professor Grace McCormack (Head of the School)
College of Science and Engineering
University of Galway

April 2023

Contents

List of Figures

List of Tables

Acknowledgements

I would like to thank my advisor Dr Nicholas Devaney for all his help in exploring this topic and domain. And to my family for all their patience as I pursued this degree.

Abstract

Electron-multiplied Charge Coupled Devices (EMCCDs) are used in many astronomical instruments where they provide much improved signal to noise compared to conventional CCDs. However, the gain provided by electron-multiplication may not be known with precision, leading to errors in the measurements. Several techniques to estimate the gain of EMCCDs are researched and investigated in this work, including some techniques previously only used for microscopy. Investigation and analyses were completed in a simulation environment, in a laboratory environment, and using data collected by an astronomical instrument (Galway Astronomical Stokes Polarimeter), where accurate gain estimation of the EMCCD detectors is important for the polarimetry results from the instrument.

Chapter 1

Introduction

Electron-multiplied Charge Coupled Devices (EMCCDs) are used in astronomical instruments where they provide much improved signal to noise compared to conventional CCDs. EMCCDs may deliver quite different gain from their nominal gains due to a variety of factors, so accurate calibration of the gain of such devices is important in order for their measurements to be useful in astronomical use cases. Accurately estimating the gain of an EMCCD is crucial for many astronomical use cases such as photometry, comparing measurements across different viewings or where the observation system has more than one EMCCD device in operation and the relative gain between the two in required, such as in the case of the Galway Astronomical Stokes Polarimeter (GASP) instrument.

In this thesis several techniques for estimating the multiplicative gain of EMCCDs are researched, and their applicability to astronomical use cases are explored. The techniques are applied in a simulation environment with synthetic data and a simulator of an EMCCD, in a laboratory environment using EMCCD devices and controlled light source conditions, and finally applied to real astronomical data collected by EMCCDs on the Galway Astronomical Stokes Polarimeter (GASP) instrument.

1.1 Background

Charge Couple Devices (CCDs) are commonly used in Astronomy as a detector for electromagnetic radiation in the visible, UV and X-ray parts of the spectrum. They were invented in Bell Labs in the late 1960s by Willard Boyle and George Smith [1]. A CCD array was first used as a detector in a telescope by Janesick [2]) in 1970, and these devices began to find broader use in astronomy in the late 1970s, as they had significant advantages over alternative electronic and photographic imaging devices including their small size, low power, linear response and excellent sensitivity over a wide range of wavelengths and light levels. A general overview of their history in Astronomy may be found in McLean [3].

A CCD is made up of an array of square-shaped light-sensitive regions arranged in a checkerboard pattern, with each square termed a “pixel” (for picture elements).

They are manufactured from a single piece of silicon. Each pixel can absorb photons of light and utilize the energy to release electrons in the semiconductor material. The level of charge is proportional to the light intensity. After the array has been exposed to the image, a control circuit causes each pixel to shift is contents to its neighbour, operating as a shift register.

CCDs have very high quantum efficiency and low dark current when operated at suitable temperatures. Under these conditions, the dominant source of noise is the readout noise, which is caused by the readout amplifier, which converts the signal in electrons into a voltage. This is in turn is then converted to an ADU (Analog-to -Digital Unit) value by an analog to digital converter. For applications where light is faint, such as with high frames rates or faint sources, the output signal can become drowned out by the readout noise.

Electron-multiplying Charge Coupled Devices (EMCCDs) were a new technology developed by e2v technologies in the early 2000s as detailed in Jerram [4], and operate in a similar manner to conventional CCDs, but with the addition of a multi-stage serial register operating at a high-voltage that produces gains in photo-electrons through impact ionisation, as shown in Figure 1.1. In this extended part of the register, the voltage used for shifting the electrons from pixel to pixel is not in the normal 5V range, but is increased to around 40 V. This increases the probability that an electron will knock another electron out of a bound state, a so-called Impact Ionisation event. The event will effectively multiply the electron. If a large number of stages are added to the extended register, an amplification of several orders of magnitude may be achieved.

This overcomes one of the main disadvantages of conventional CCD detectors, namely read noise, by multiplying the electrons before being read out to such a degree that single photon-generated electrons may be detected. This enables EMCCDs to produce images at high read speeds and at low light levels, without being overwhelmed by readout noise.

Early exploration of potential applications for the use of EMCCDs in Astronomy were first explored in Mackay [5], and they have since been used in many astronomical instruments. Some notable examples have been the QUCAM2 instrument at the 4.2-m William Herschel Telescope [6] and ULTRASPEC instrument at the ESO 3.6m telescope at La Silla [7].

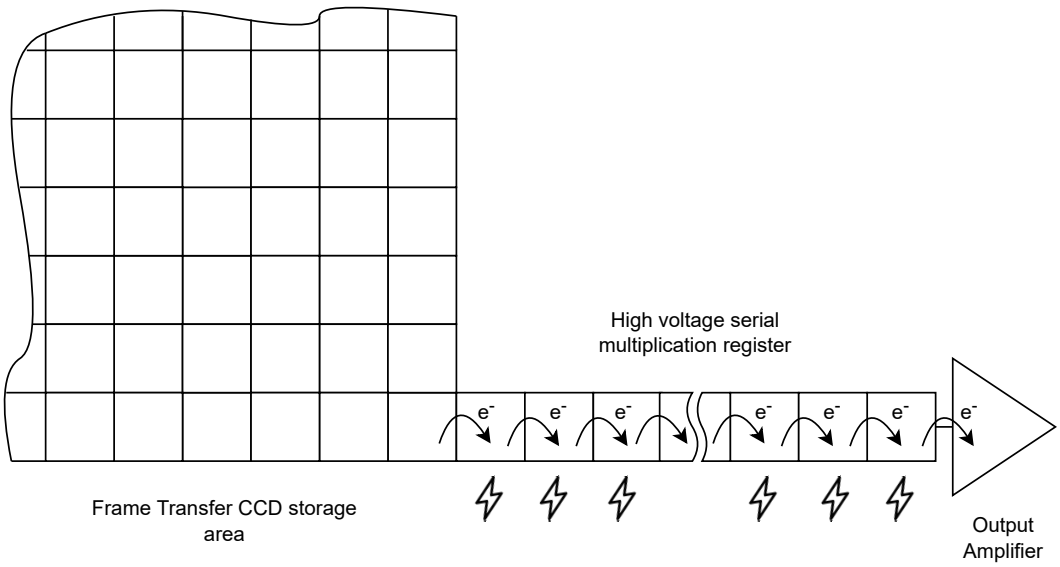

Figure 1.1: Schematic showing the extended register on an EMCCD. After exposure and parallel shifting into the storage area, the image is read out serially. The extended high voltage serial multiplication register generates cascade amplification via impact ionisation (Image by author)

Modelling the Amplification Process

In order to develop or apply any gain estimation methods, a model of the multiplicative gain mechanism in the EMCCD device along with models for the various noise mechanisms in the device is required. In this section, a basic model will be outlined, as developed in the wider literature.

Due to the probabilistic nature of the gain mechanism, the number of electrons resulting from one photo electron is not constant. The gain of the electron multiplying register is random for individual input photo electrons, similar to an avalanche photodiode or a photo-multiplier. The output distribution of data will not be normally distributed, and indeed follows a more complex distribution.

According to Basden [8], assuming each individual register in the EM serial register has a probability P_m of producing an extra electron, the gain for m steps may be given by:

$$\gamma = (1 + P_m)^m \tag{1.1}$$

If we let X be a random variable representing the number of electrons resulting from one input electron propagating through the EM register, the probability den-

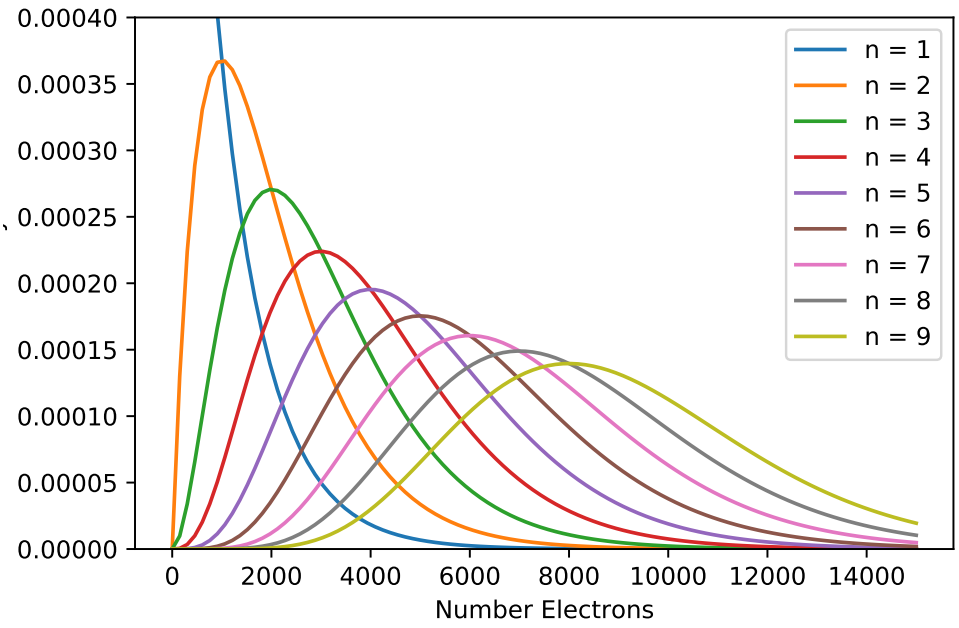

Figure 1.2: A set of Gamma probability density functions as defined in equation (1.3) for n={1,2,3,4,5,6,7,8,9} and $\gamma = 1000$

.

sity function of X is given by:

$$P(X = x) = \frac{1}{\gamma} e^{-x/\gamma} H(x) \tag{1.2}$$

where H is the Heaviside function, which is the integral of the δ function. The γ parameter is the EM amplification. If we take the scenario of n input electrons, the resulting output distribution of the X output electrons is given by an Erlang distribution given in Equation 1.3 below. This is a specific version of a Gamma distribution when n may only take on integer values. The derivation of Equation 1.2 and Equation 1.3 may be found in Basden [8]

$$P(X = x|n) = x^{n-1} \frac{e^{-x/\gamma}}{\gamma^n \Gamma(n)} \tag{1.3}$$

The distribution has an expectation value of $n\gamma$ and variance of $n\gamma^2$. As n gets very large, the distribution converges to a Gaussian distribution also with an expectation $n\gamma$ and variance $n\gamma^2$.

The distributions for different n values have large overlaps, as shown in Figure 1.2, so using just the readout value, it is not possible to determine how many input electrons caused it with absolute certainty

The distribution above has a mean value of $n\gamma$. If the EMCCD is operated like any other CCD, after exposing the array for a certain period of time t, the output value could be divided by $n\gamma$, which would provide an estimate for the number of photons. However this introduces an additional noise on top of photon shot noise, referred to and the Excess Noise Factor (ENF). Assuming an average of k photons hit a pixel in the EMCCD device, the resulting signal to noise ratio will be:

$$S/N = \frac{\gamma k}{\sqrt{\sigma_{shot}^2 + \sigma_{EM}^2}} = \frac{\gamma k}{\sqrt{\gamma^2 k + \gamma^2 k}} = \frac{k}{\sqrt{2k}} \tag{1.4}$$

The Excess Noise Factor effectively lowers the Quantum Efficiency (QE) of the EMCCD, in that twice as many photons are required to achieve a given S/N.

There is additive noise added to the output signal as a result of the readout electronics. This readout noise may be modelled by the random variable R following a Gaussian distribution with a bias b and standard deviation σ, given by:

$$P(R = x) = \mathcal{N}(x - b, \sigma) \tag{1.5}$$

where $\mathcal{N}$ is a normal distribution. One approach to estimating the gain is to capture a set of calibration images, where we can be sure they are so faintly illuminated that no more than one electron enters the multiplicative register. It this case, the random variable S representing the number of output electrons is a sum of the two random variables above:

$$S = X + R \tag{1.6}$$

Adding two independent random variables together results in a convolution of their respective probability distribution functions (PDFs). If we ignore the width of the normal distribution when it is convolved with the exponential distribution, and due to the width of the latter when the EM gain is sufficiently high, we can rewrite the resultant distribution as in Harpsöe [9] as the following mixture model:

$$P(S = n) \approx p\mathcal{N}(x - b, \sigma) + (1 - p)(x^{n-1}\frac{e^{-x/\gamma}}{\gamma^n \Gamma(n)})H(x - b) \tag{1.7}$$

If we make the assumption that the image is weakly illuminated, never exceeding 1 photon per pixel, this simplifies to:

$$P(S = n) \approx p\mathcal{N}(x - b, \sigma) + (1 - p)(\frac{1}{\gamma}e^{-x/\gamma})H(x - b) \tag{1.8}$$

where $H(x - b)$ is a Heaviside function. Equation 1.8 provides a simple model for distribution of the EMCCD output values under faint illumination, and can be used to estimate the gain of the device, as detailed in the next chapter. However there are additional processes that need to be modelled in the EMCCD in order to produce a more accurate model.

In addition to the multiplicative gain from impact ionization, there are other sources of noise produced as part of the shift-out process. Spurious charges caused by the clock induced charge (CIC) phenomenon will appear at the outputs, even in dark images. Spurious electrons may be generated in three places in the EMCCD: in the parallel register (which shifts out a row of the EMCCD charge packets in parallel), in the serial register (responsible for transferring the charge packets one by one in a sequential manner from the parallel register to the device's EM register) and in the serial electron multiplication (EM) register (purpose is described previously).

Spurious charges are not important in the context of conventional CCDs, as they are normally not noticeable in the presence of the readout noise. However in an EMCCD these spurious electrons will be amplified in the EM register, resulting in a noticeable contribution to the output signal. According to Harpsöe [10] the spurious electrons from the serial register are indistinguishable from the spurious electrons generated in the parallel registers, and are much less frequent, so can be ignored in the modelling. The spurious electrons in the parallel registers are defined here as parallel clock induced charge (pCIC). The other important source of spurious electrons are those which arise in the EM register, which are defined here a serial clock induce charge (sCIC). While the pCIC is indistinguisable from actual photoelectrons, this may not be the case for sCIC, as these electron may travel a shorter length through the register depending on where they arise, which results is a lower overall gain.

Mathematically, if a spurious electron enters the EM register at the k'th stage it can be modelled as a random variable X_k, where:

$$P(X_k = x) = \frac{1}{\gamma_{m-k}}e^{-x/\gamma_{m-k}}H(x) \tag{1.9}$$

In order to build a model of the output distribution that models the above processes, a few terms need to be defined. In the case where no electron enters the EM multiplier we assume there is a constant bias reading as the probability distribution of the bias reading is:

$$P(B = x) = \delta(x) \tag{1.10}$$

Define R as the readout noise modelled by:

$$P(R = x) = \mathcal{N}(x, \sigma) \tag{1.11}$$

p_s is the probability a sCIC electron arises in one of the multiplier steps. p_p is the probability a pCIC electron arises in a parallel register. As the probability of multiple pCIC or sCIC electrons is low, we can assume that the probability that multiple sCIC and pCIC electrons and coincident pCIC and sCIC electrons is negligible. This assumption allows the following for the total output Z of a bias reading as a mixture distribution:

$$Z = \left\{ \begin{array}{l} \text{B with } 1 - p_p - mp_s \\ \text{X with } p_p \\ X_k \text{ with } p_s \end{array} \right\} + R \tag{1.12}$$

As above, if we assume a sufficiently high gain, the complex convolution can be simplified resulting in the following expression:

$$P(Z = n) \approx (1 - p_p - mp_s)p\mathcal{N}(x - b, \sigma) + (\frac{p_p}{\gamma}e^{-x/\gamma} + \sum_{k=1}^{m} \frac{p_s}{\gamma}e^{-x/\gamma})H(n) \tag{1.13}$$

While the model above was derived in Harpsöe [10] for bias readings, it could also be used for extremely faint exposures were the pCIC levels can be considered a proxy for real photo electrons, as they are indistinguishable, as noted above. These output distribution models will form the basis for the estimation techniques outlined in the next chapter.

1.2 Literature Review

A literature review was carried out to understand the state of the art in the field of Electron-multiplied Charge Coupled Device (EMCCDs) usage for astronomical work, and specifically gain estimation techniques and their application to astronomical use cases. Techniques for post-processing EMCCD data to improve the quality of astronomical results were also investigated, as this may be applicable to some of the GASP data. The estimation techniques themselves will be discussed at a

high-level in this review, and will be explored further in the relevant sections of the thesis.

Since their introduction in the late 1990s, there has been a fair amount of research and literature on the topic of accurately modelling the behaviour of EMCCDs, and developing methods to accurately calibrate them. A general overview of the use of electronic imaging devices in astronomy may be found in McLean [3]. This gives a broad background on the evolution of electronic imaging devices in telescopes, providing detailed explanations of the practical operation of CCDs in telescopes, along with techniques for their characterization and calibration. While EMCCDs are mentioned in this text, they are not a specific focus of the work.

One approach detailed in McLean [3] is to utilise the Photon Transfer Curve of the device to estimate the gain of a CCD. This is commonly referred to as the 'Variance Method' or 'Photon Transfer Method' in the wider literature. A noise model is developed for a standard CCD, and this calibration method then leverages the relationship between the mean of the output signal to its variance to determine the overall gain of the CCD from input photon to output digital value. This method works by applying the photon transfer curve (PTC) to a series of data of varying intensity levels. An example of a PTC from a CCD device may be seen in Figure 1.3, taken from Hirsch [11], where the author collected output data points at nine different discrete input intensity levels. At this part of the curve shown, a linear relationship may be observed between the mean and variance. Special consideration needs to be taken to ensure that the field is flat. Manufacturers and researchers typically make use of this calibration method because it is easy to implement. However, as the text details, it requires a flat input field and several fixed illumination levels. While this may be suitable for a laboratory environment this may not be practical or possible at a telescope.

In order to understand how to model the specific behaviour of an EMCCD, some more foundational works specific to EMCCD modelling and operation were researched. Early work on the modelling and simulation of EMCCDs, done shortly after their invention and use in astronomy, is presented in Tubbs [12]. The author proposed two models for the multiplicative process in the output serial register, and also developed a simulator to test out the models and compare the resulting output distribution with real astronomical data. The astronomical data was found to be generally consistent with the simulations. Because of the computation and memory required to simulate potentially millions of electrons in a Monte Carlo simulator,

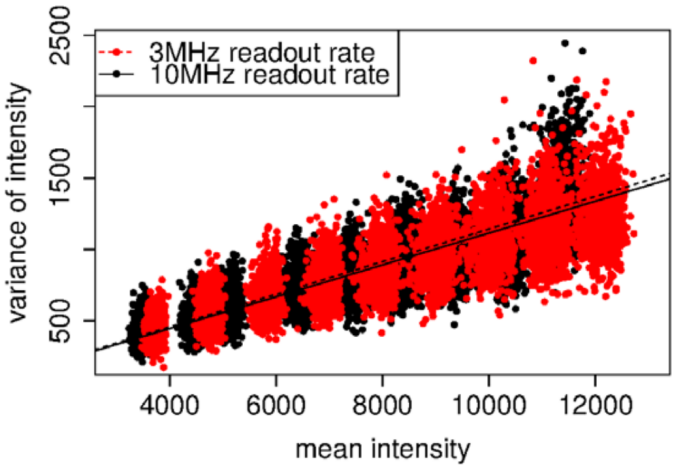

Figure 1.3: A experimental PTC taken from Hirsch [11] for 9 input light intensities. Each dot represents mean and variance of the intensity of an individual pixel for 60 frames across a single data set. The values of the 9 data sets are shown which appear as "blobs" in the figure. (The author utilised two different readout rates, which do not impact the PTC curve)

.

the author uses Discrete Fourier Transforms (DFTs) to model the convolutions in the probability models required to simulate multiple electrons as multiplications in the Fourier domain. It was noted that this reduced the computation requirements considerably.

Further analysis of the performance of EMCCDs was undertaken in Basden [8], where techniques were explored to reduce the effect of the noise introduced by the multiplicative gain process. For high gain the signal-to-noise ratio of the output signal in an EMCCD can be reduced by a factor of $\sqrt{2}$ due to a so-called Excess Noise Factor (ENF), so post-processing techniques using thresholding are explored to mitigate this. The work uses a similar but slightly different model to Tubbs [12] and formally derives the output probability distribution to be a Gamma Distribution. To validate the model and thresholding techniques, a Monte Carlo simulation of the EMCCD is undertaken.

Tulloch [13] adopts the model from Basden [8], but additionally explores the effects of Clock Induced Charge both before and in the EM register. As there is no derivation of the output probability distribution that includes the effects of clock induced charge, a Monte Carlo simulation is undertaken that incorporates this effect. Also in this work is detailed a means to estimate the gain of the EMCCD by fitting a

line to the log of the output histogram of the faintly illuminated detector and using the slope to estimate the gain. Referred to in this research as the 'Exponential Slope Method', this method is possible because the complex Gamma distribution simplifies to an exponential distribution at a flux rate of a maximum of one photon per frame. This method is also detailed in Harpsöe [9], where the author applies it to calculate per pixel parameters including gain for an EMCCD. In Harpsöe [9], the author is able to simplify the model, which also includes Gaussian readout noise, further to a mixture distribution, provided the EM gain is sufficiently high, allowing the standard Expectation Maximization (EM) algorithm to be used to estimate the parameters. The same author's other work [10] derives an output probability distribution that includes the effect of Clock Induced Charge, using the same mixture assumption.

A much more complete modelling of the stochastic behaviour of EMCCDs is derived in Hirsch [11]. The domain of the authors is not astronomy but biological science using microscopy, which is another area where EMCCDs are used widely, and where there is more active research on their use in recent years. A model of the full noise process, taking into account the Poisson sampling of the incident light at the input, modeling the EM register using the same Gamma model derived in Basden [8], and incorporating a Gaussian model for the readout noise, is derived. Also included are techniques to estimate all the parameters of the model in a laboratory setting. For gain estimation, these are similar to the methods outlined in McLean [3] for regular CCDs, but incorporate the Excess Noise Factor (ENF) already mentioned above that needs to be accounted for when using EMCCDs.

An advancement of this general technique for estimating the gain on an EMCCD in a laboratory calibration setting has been developed in Ryan [14]. It notes that the 'Variance Method' requires many measurements per set-point that are time-consuming to obtain, and states that researchers will typically make use of several gain settings depending on experimental conditions to obtain optimal signal levels. This can be particularly inconvenient because voltage degradation in the amplification register requires periodic re-calibration. As the 'Variance Method' is based on linear regressions, its parameter estimation and uncertainty analysis reflect the implied noise of measuring the means and variances from each dataset. Covariances among parameters are not accurately addressed, potentially leading to the mis-characterisation of parameters and their uncertainties. In Ryan [14], the author defines a method that characterizes multiple detector parameters in fewer measurements and with improved accuracy by introducing a probabilistic calibration method

for determining the gain parameters, using an EMCCD noise model very similar to the one in Hirsch [11]. This method develops a Maximum Likelihood Estimation (MLE) technique that can be applied to an Intensity-Series of fixed intensities, or a Gain-Series of different nominal gains set on the EMCCD. The techniques developed were applied in the field of microscopy.

While methods that require explicit calibration data collection are useful in a laboratory setting, even more useful are techniques that can estimate the device parameters from the acquired images themselves. This eliminates the need for separate calibration data, and ensures that any changes in gain due to the environment are also accounted for.

O'Connor [15] uses the 'Exponential Slope Method' detailed above on regular Astronomical data from the GASP instrument and notes that it is important to only use a region of the sensor that is faintly illuminated, such as background sky, so that the exponential distribution assumption outlined above can be made.

It was noted during the literature review that a large amount of the research into EMCCD calibration techniques is on-going in the microscopy field, so it was interesting to see if these new techniques could be applied to Astronomical data. A unique new approach that allows estimation of the EMCCD gain without the need for explicit calibration sets is the Calibration-On-The-Spot (COTS) method developed in Mortensen [16]. Rather that relying on faint images where the exponential distribution assumption may be made, this approach assumes that we are observing a source that has a flux rate high enough such that the detector output distribution is well approximated by a Gaussian. In addition, it is assumed that the signal intensity falling on the imaging array corresponds to a known point spread function (PSF). The gain and other parameters may be recovered using Maximum Likelihood estimation once these assumptions are valid. While the first assumption with respect to high photon counts may be satisfied when using this method in Astronomy, the known PSF assumption is more difficult for ground-based telescopes due to the seeing effects of the atmosphere. While Mortensen [16] uses a 2-D Gaussian as the point spread function, it was noted that in long-exposure Astronomy, a so-called Moffat Distribution [17] is the commonly used model.

As it was clear that the research for this thesis would require the software development of data processing algorithms for application to real data from the detector, and also the requirement to write software that could simulate astronomical light sources, the effects of atmospheric seeing, and the simulation of photo electrons get-

ting multiplied in EM register, some research was carried out on available software packages that could be used. As the author was familiar with the Python language, the packages in this language were research and selected. Astropy [18], an extensive package for Astronomy data processing was selected for general use, and it provides libraries for handling astronomical FITS files, fitting common source models amongst other useful features. In order to simulate the atmospheric seeing effects, the library AOTools library detailed in Townson [19] was researched. Interesting features in this include the simulation of atmospheric turbulence phase screens. After some research, the author was unable to find any packages or source code from previous works that could simulate an EMCCD itself, so it became apparent this would need to be written from scratch.

Chapter 2

Proposed Methods

In this thesis a number of methods for estimating the gain of the EMCCD are proposed and investigated, and they are detailed in this section. In the following chapters, they will be explored further in a laboratory setting, in simulation, and finally some of them are applied to estimate the gain in data obtained using the Galway Astronomical Stokes Polarimeter (GASP) at the 8 m Gemini telescope.

2.1 Histogram Slope

Given a set of output pixel samples from recorded images that are faintly illuminated, the distribution in Equation 1.8 provides a simplified output distribution model. As the log of an exponential will be a straight line, a least squares fit of the linear part the log of the output distribution, as seen in Figure 2.1, may be used to estimate a slope, which in turn will provide an estimate for the γ of the exponential distribution, which represents the EM gain of the device. This method was used by O'Connor in [15]. Suitable values for the start output value, O_s, and end output value O_f, need to chosen which represent the bounds of the linear region, within which the histogram values may be used as input to a least-squares line fit. In order to get a value for O_s, a common method is to take an offset from the estimated mean, μ of the readout noise Gaussian, where the magnitude of the offset is a multiple of the estimated σ. Typically a value of 5.5 in Daigle [20] or 6 in O'Connor [15] is used. The purpose of the offset is to avoid the non-linearity in the log output, particularly due to sCIC described in the previous section. There are different techniques to estimate the σ and μ parameters. While the method in O'Connor [15] to determine these is not detailed, the approach taken in this thesis is to use the Expectation Maximisation (ExpMax) algorithm to first estimate the Normal distribution of the mixture in Equation 1.8, as ExpMax was already going to be implemented for the next method detailed in Section 2.2 below. There were no obvious techniques documented in the literature for choosing a suitable end output value O_f. Picking too large a value will move the linear fit into a region of output values where where there are very few counts per bin and therefore large uncertainty or other non-linearities not captured by the model assumptions. This can be seen in real EMCCD data shown in Figure

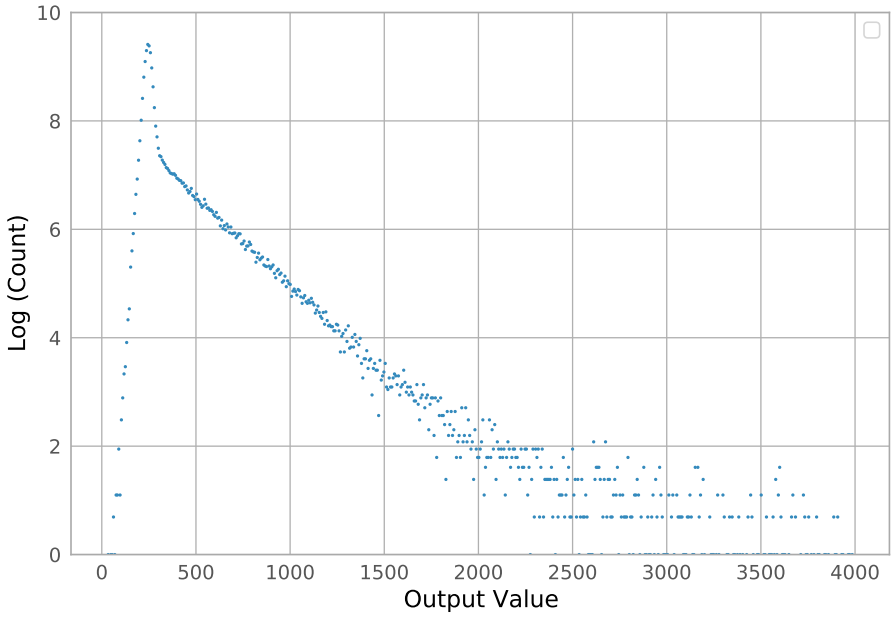

Figure 2.1: Sample output histogram taken from high-speed data recorded by an EMCCD detector in the Galway Astronomical Stokes Polarimeter (GASP) during observation of the Crab Nebula.

.

2.1, where the curve appears linear between output values 500 and 1500, but non-linear outside of this region. Techniques for choosing these values will be explored further in the following chapters.

The accuracy of an EM gain estimate using this method is subject to a number of key assumptions:

- The EM gain is sufficiently high to justify the mixture approximation.
- The input source is faint enough so that no more than one photon is received per frame on any pixel also taking into account any pCIC contribution
- Other noise mechanisms in the EMCCD such as serial sCIC electrons that cause spurious charges may be ignored or minimized with a choice of O_s

Along with needing to satisfy these assumptions, another drawback of this approach is the need for a set of faint calibration images being captured in advance of the astronomical viewing, or having to identify sufficiently faint regions to be extracted

from astronomical images. The former limits observing time and the gain may also drift post calibration, as the electron generation processes are highly dependant on the voltage level applied to the serial register, the environmental temperature of the device (as mentioned in Hirsch [11]), and the age of the device, with the gain decaying over time (as mentioned in e2v technologies [21]. The latter may erroneously assume regions of the image selected for use in the histogram were subject to faint illumination, as it is not possible to uniquely determine the input photon count from the measured output.

2.2 Fitting EMCCD noise model parameters

Given a set of output pixel samples from recorded images that are faintly illuminated, the distribution in Equation 1.8 may be fitted to recover its parameters, one of which is the EM gain of the device. Additionally, the more complex model that incorporates the Clock Induced Charge phenomena represented by Equation 1.13 may also be fitted. In order to recover the parameters of either model from the data, the Expectation Maximization algorithm is utilised (abbreviated in this text to ExpMax to avoid confusion the Electron Multiplication). This is a standard method for estimating the parameters of a mixture distribution. The ExpMax algorithm is also applied to the histogram of pixel values, just like the previous algorithm.

The ExpMax algorithm is an iterative method for model parameter estimation with the latter dependent on unobserved latent or 'hidden' variables. In this case we do not know which samples belong to which distribution in the mixture. The ExpMax iteration alternates between performing an expectation (Exp) step, which creates a function for the expectation of the log-likelihood evaluated using the current estimate of the parameters, and a maximization (Max) step, which computes parameters maximizing the expected log-likelihood found on the Exp step. These parameter-estimates are then used to determine the distribution of the latent variables in the next Exp step. For the model in Equation 1.8, the probability λ_i of a sample belonging to the normal component of the mixture is estimated in the expectation step according to this equation derived in Harpsöe [9]:

$$\lambda_i = \frac{\hat{p}\mathcal{N}(n_i - \hat{\mu}, \hat{\sigma})}{\hat{p}\mathcal{N}(n_i - \hat{\mu}, \hat{\sigma}) + (1 - \hat{p})(\hat{\gamma} e^{\hat{\gamma}(n_i - \hat{\mu})})} \tag{2.1}$$

In the maximization step, the maximum likelihood estimates of all the parameters are calculated with the following update equations:

$$\hat{p}_{k+1} = \frac{1}{M} \sum_i \lambda_i \tag{2.2}$$

$$\hat{\mu}_{k+1} = \frac{\sum_i \lambda_i (n_i - \hat{\mu_k})}{\sum_i \lambda_i} \tag{2.3}$$

$$\hat{\sigma}_{k+1} = \sqrt{\frac{\sum_i \lambda_i (n_i - \hat{\mu_k})^2}{\sum_i \lambda_i}} \tag{2.4}$$

$$\hat{\gamma}_{k+1} = \frac{\sum_i 1 - \lambda_i}{\sum_i (1 - \lambda_i)(n_i - \hat{\mu_k})} \tag{2.5}$$

where $\hat{\mu}$, $\hat{\sigma}$, and $\hat{\gamma}$ are the parameters of the model previously defined in Equation 1.8.

The algorithm in sensitive to starting parameters and can converge to local optima if these are not initialised correctly. The equations above were updated to accommodate the extra parameters of the more complex model in Equation 1.8, and while omitted here for brevity, may be found in the source code for the algorithm implementation detailed in the references. Both estimation algorithms (simple and complex model) were implemented in Python and included in the Appendix, and validated with sample mixture data. Using the equations above, estimates for the model based on the output data may be found if the algorithm is executed until convergence.

It requires the same assumptions with respect to a faint source and high gain as the previous algorithm in order to get a good results, but since it models the sCIC of the device, it may produce better results which will be tested later in this work.

2.3 Calibration-on-The-Spot (COTS)

An alternative approach by Mortensen [16], that eliminates the need for separate calibration images to estimate the gain, has been applied in the microscopy domain. This approach is referred to as "Calibration-On-The-Spot" (COTS). Rather than relying on faint images where we can make the exponential distribution assumption, this approach assumes that we are observing a source that has a photon rate high enough such that the detector output distribution is Gaussian, as was shown previously in Figure 1.2 with increasing photon rates. In addition, the method assumes that the signal intensity falling on the imaging array corresponds to a known point

spread function (PSF). According to the COTS formulation, if we have a number n of photons detected by a given pixel that is modelled as a Poisson distributed random variable, we denote the expected value v as:

$$E(n) = v \tag{2.6}$$

As previously, for each photon detected in a given pixel, the EMCCD will output a random number of electrons S, which can be modelled by an Erlang distribution previously derived in Equation 1.3. In the COTS formulation, advantage is taken of the fact that the output distribution approaches a normal distribution as the input signal v increases. As previously, the output also typically has a fixed bias added that may be modelled by b. With these assumptions, the author derives the first two central moments of S from its output distribution as:

$$E(S) = \gamma v + b \tag{2.7}$$

and:

$$Var(S) = 2\gamma(E(S) - b) \tag{2.8}$$

where γ is the gain. For each pixel in the image, we assume the measured output, S, is normally distributed around it's mean output value with a variance given by Equation 2.8. Since we do not know the true mean value of the output signal in Equation 2.7, we can replace this with a value obtained by fitting the data to a known PSF, and using the resulting model to determine the expected signal values for any pixel. The Gain and Offset can then be recovered using Maximum Likelihood Estimation (MLE) with respect to the parameters using Equation 2.8. Details of this MLE formulation may be found in Mortensen [16]

While single pixels will provide poor gain estimates, the method can provide a robust means of estimating gains if many pixels are used across many frames. While the first assumption with respect to high photon counts may be satisfied when using this method in Astronomy, the known PSF assumption is more difficult for ground-based telescopes due to the effects of atmospheric turbulence (seeing).

The COTS approach in Mortensen [16], assumes diffraction-limited images where the PSF may be approximated by a Gaussian, and a localisation algorithm is used to fit a 2-D Gaussian to the isolated microscopic probes used in that domain. However, in astronomy, seeing causes short-exposure images to have a complex, speckle structure, and only long-exposures might follow a smooth PSF. For large diameter

telescopes, a short duration integration of the source will follow a speckle pattern, due to atmospheric turbulence. Over longer integrations, the PSF will take the form of a 'seeing disk', the size of which depends on the seeing condition.

While the cores of such long-exposure images have a Gaussian shape, the wings are found to be better approximated with a Moffat [17] profile. In addition, different effects can cause deviations from a Gaussian shape – including optical aberrations, and telescope vibrations. The 2-D Gaussian approach was used in Mortensen [16], and as the core of the PSF is most important for this method, being the region where the high flux assumption holds true, the Guassian model will also be used here when applying this method.

2.4 Photon Transfer Curve Mean-Variance (MV) Technique

The gain estimation technique using the Photon Transfer Curve is also known as the mean-variance (MV) technique. It was originally developed to estimate the parameters of a regular CCD. It involves taking a set of exposures of a flat field with different illumination levels. Dark exposures are also taken and subtracted to remove fixed pattern noise and bias. From the exposures we can estimate the mean S and variance V of the output signal data X_i:

$$S = \frac{1}{n} \sum X_i \tag{2.9}$$

$$V = \frac{\sum (S - X_i)^2}{n - 1} \tag{2.10}$$

where n is the number of pixel samples. While CCDs do not have multiplicative EM gain, along with EMCCDs, they do have another gain parameter g, the A/D proportionality factor, which represents the gain of the analogue to digital process, or more specifically the number of electrons per output value. If we turn off the EM gain on an EMCCD, so that is behaves like a regular CCD, the output noise should have two primary sources:

- Photon noise on the signal photoelectrons σ^2_{shot}
- Readout noise from the output amplifier $\sigma^2_{readout}$

The two noise sources are independent, and may be added together, such that the output noise is:

$$\sigma^2_{output} = \sigma^2_{shot} + \sigma^2_{readout} \tag{2.11}$$

The above expression applies to photo-electrons. The measured quantities above, the mean signal S and its variance V, are in output units or Data Numbers (DN) as it is often termed. The expression for the variance using DN is:

$$(\frac{\sigma_{output}}{g})^2 = (\frac{\sigma_{shot}}{g})^2 + (\frac{\sigma_{readout}}{g})^2 \tag{2.12}$$

where g is the A/D proportionality factor mentioned above. The left-hand side is now V, the observed variance in DN. The mean number of photoelectrons is gS, so noise on this number from Poisson statistics give σ^2_{shot} as gS. The equation therefore simplifies to:

$$V = \frac{1}{g}(S) + (\frac{\sigma_{readout}}{g})^2 \tag{2.13}$$

This is the equation of a straight line in a signal-variance plot where x=S and y=V. Therefore, the A/D factor, g, can be estimated as the inverse of the gradient of the least-squares straight line fit to the mean-variance data, combining results from multiple intensities. Ignoring the constant term, we can rewrite the estimator for g as simply:

$$\hat{g} = \frac{S}{V} \tag{2.14}$$

The above equation does not hold for EMCCDs. At high EM gains, the readout noise is negligible, but we need to take into account the excess noise factor previously discussed. Hirsch [11] derives a similar expression for the estimated EM gain, λ, in terms of the estimated output mean S and variance V:

$$\hat{\lambda} = g\frac{V}{2S} \tag{2.15}$$

Hence, we can estimate λ through a mean-variance test of stacks of images with different intensities, fitting a straight line and using the gradient.

2.5 Maximum Likelihood Intensity Series and Gain Series

Ryan [14] proposes a method that use Maximum Likelihood Estimation (MLE) to estimate the parameters of the output noise model, based on the observed data. The author uses the Poisson-Gamma-Normal (PGN) noise model derived in Hirsch et al. [11]. While the full expression may be found in Hirsch, it can be represented in terms of its parameters as:

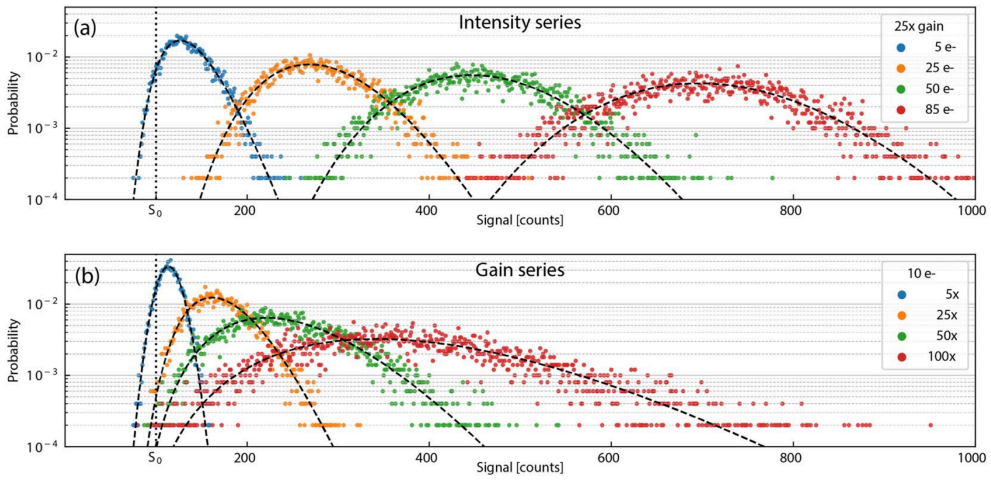

Figure 2.2: These figures taken from Ryan [14] show what sample datasets for the IS and GS MLE methods would look like. (a) The first shows a simulated set of IS calibration samples for multiple intensity values, where the EM gain remains constant across each set. Histograms of simulated samples at 25× gain (colored markers) and their corresponding PDFs (dashed lines) for four intensity levels are depicted. (b) Shows the simulated histograms and PDFs for four gain levels representing a common intensity of 10 photoelectrons. The IS and GS depicted were simulations of 5000 samples, with σ = 10, b = 100 counts, and ADU = 3.5 e/count

.

$$p(S|E, g, \lambda, b, \sigma) = q(S|E, g, \lambda) * N(S|b, \sigma) \tag{2.16}$$

where * is the convolution operator, $q(S)$ represents the Poisson-Gamma noise distribution and $N(S)$ represents the normally distribution readout noise. The parameter S is the output signal, b is the bias, E is the number of input photo electrons, g the ADU gain, and λ the EM gain, with σ the standard deviation of the readout noise.

The Intensity Series (IS) and Gain Series (GS) probabilistic calibration methods use MLE to group multiple intensity datasets (for ADU or EM gain calibration) or

multiple gain datasets (for gain calibration only) together with shared parameters using a global log-likelihood function:

$$ln\mathcal{L}^{global} = \sum_{i=1}^{M_{max}} \sum_{i=1}^{N_{max}} ln\mathcal{L}(S_j^i | p^{(i)}) \tag{2.17}$$

where M_{max} is the number of individual datasets in the series, N_{max} is the number of samples (frames) in an individual series, and $p^{(i)}$ represents the combined set of common parameters and unique parameters for a given dataset in a series. The model parameters for each probabilistic calibration method are summarized here:

$p(i) = \{E(i), \lambda = 1, g, b, \sigma\}$	For IS MLE calibration to estimate g
$p(i) = \{E(i), \lambda, g, b, \sigma\}$	For IS MLE calibration to estimate λ
$p(i) = \{E, \lambda(i), g, b(i), \sigma(i)\}$	For GS MLE for gain calibration to estimate λ

Optimization is used to find parameter estimates that maximize the global log-likelihood function. The author used the Broyden–Fletcher–Goldfarb–Shanno (BFGS) optimization algorithm in their implementation, but others could also be used. As there is no analytical solution for Equation 2.16, the author uses the Fast Fourier Transform (FFT) to compute the convolution as part of evaluating the likelihoods. A simulation of the type of calibration data that would be used in the IS MLE and GS MLE algorithms may be seen in Figure 2.2

Chapter 3

Simulation Results

In order to test out and validate the different methods before applying them to real data, a simulation environment was developed. This included simulating the astronomical sources, the seeing processes occuring in the atmosphere before the light reaches the detectors, and then the various processes on the EMCCD device, including the electron multiplication and noise processes modelled in the previous chapters.

3.1 Astronomical Source Simulation Set-up

Sample images representing the flux incident on the EMCCD detector caused by point sources were generated using different numerical simulations. All the code to generate the input is detailed in Appendix A

Flat field simulation

Flat fields were generated by setting a fixed number of photons to each pixel of the input array. Individual photon counts for each pixel of each simulated flat input frame could also be Poisson sampled independently, in order to simulate the shot noise.

Sources Using Gaussian and Moffat PDFs

Simple Gaussian and Moffat sources, which can serve as simple models for point astronomical sources after a long exposure, were generated using the analytical probability density functions (PDFs) for those 2-D distributions. The Gaussian model represents a good first-order approximation for a diffraction limited scenario, whereas the Moffat distribution more accurately reflects the effects of atmospheric seeing after a long-exposure. The latter distribution has the following probability distribution function (PDF):

$$p(x, y; \alpha, \beta) = \frac{\beta - 1}{\pi \alpha^2} \left[1 + \left(\frac{x^2 + y^2}{\alpha^2} \right) \right]^{-\beta} \tag{3.1}$$

where α and β are the seeing dependent parameters which determine the width and

shape of the distribution respectively

Images generated from the PDFs could then be weighted for an overall target photon number per frame. Individual photon counts for each pixel of each simulated input frame could also be Poisson sampled independently, in order to simulate the shot noise.

Simulating Atmospheric Seeing

A more complex simulation was undertaken to simulate the astronomical seeing process with more accuracy than using the simple PDF models of the previous section. Without seeing effects, observed images are typically diffraction limited. This results in the images of point sources following an Airy pattern, whose core can be further simplified and modelled as a simple 2-D Gaussian, as described already in this chapter.

However, atmospheric turbulence causes the images to break up into speckle patterns, which change very rapidly with time. An extended exposure of these speckle patterns will result is a blurred image of the point source, which is known as a seeing disc. This seeing disc can be approximated with a Moffatt distribution, as mentioned above. A common model used in astronomy to model the effects of the atmosphere is the Komologorov turbulence model, an overview of which can be found in McLean [3], and further detail in Quirrenbach [22]. A detailed explanation may be found in those texts and is beyond the scope of this thesis, but some key points are summarized here.

In a turbulent atmosphere using this model, different parts of the air have different indices of refraction, and cause different phase delays across wavefronts passing through it. When the light finally arrives at a telescope, the wave-front is not flat, and the rays are no longer parallel. The spatial structure of the atmosphere in this model is described statistically in terms of a structure function $D(r)$, which gives the difference in refractive index squared between two points separated by a distance $r = (r_1 - r_2)$, whose formulation described in McLean [3] for Komolgorov turbulence is given by:

$$D_n(r) = \langle |n(r_1) - n(r_2)|^2 \rangle = C_n^2 r^{2/3} \tag{3.2}$$

The factor C_n^2 measures the strength of the turbulence. The stellar wavefront incident on the telescope has spatial variations in both amplitude and phase. The

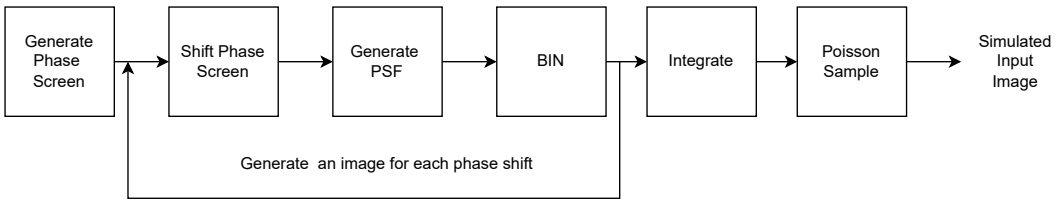

Figure 3.1: Process used to simulate input images for sources undergoing atomospheric seeing effects

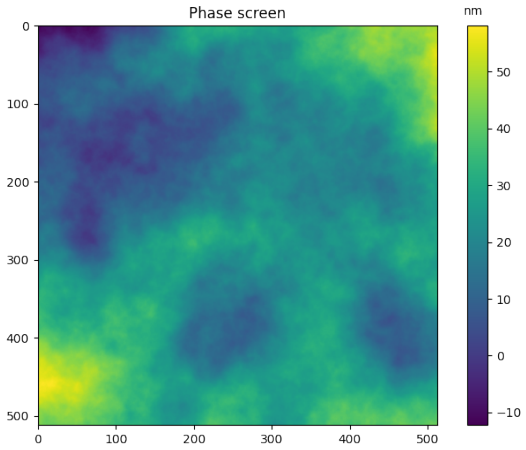

Figure 3.2: An example phase screen generated using the AO-Tools library. In this case, the configuration is screen size = 512, D (telescope diameter) = 8 metres, r_0 (Fried Parameter) = 0.164 metres, L0 (Outer scale) = 50 metres, wavelength = 500 nanometres

amplitude variations cause scintillation (more commonly observed as 'twinkling') and contribute much less to image quality degradation than the phase variations. By finding the effect of the thin turbulent layer on an incident plane wave, it is possible to derive a structure function for phase variations and then integrate this through the atmosphere. By doing this integration, the phase structure function D_ϕ over the entrance of a telescope for Kolmogorov turbulence is derived in Quirrenbach [22] to be:

$$D_\phi(r) = 6.88(r/r_o)^{5/3} \tag{3.3}$$

The important parameter in this equation is the Fried parameter r_0, which is the length over which the wavefront is not significantly perturbed.

The AOtools library described in Townson [19] was used to simulate Kolmogorov Phase Screens. An individual phase screen can be shifted for each frame to simulate wind-driven motion of the turbulence during observation, and then for each frame, the phase screen may be converted into an image on the detector by multiplying the phase screen by the telescope aperture mask, and then transforming it to the focal plane using a Fourier transform. Images could be subsequently binned spatially to represent different pixel scales. Multiple images could be integrated to represent different integration periods. This process is summarized in Figure 3.1

In order to ensure that the AOTools library was generating phase screens in line with the Komologorov theory, an analysis was completed to see if the phase screens obeyed Equation 3.3. Firstly, to estimate the structure function, 1000 phase screen were generated, and radial rings from the center were used to estimate phase differences at different distances from the center. The results may be found in Figure 3.4. While the structure function does follow the expected power law from Equation 3.3, it does so for a larger r_O than the one simulated.

Another means of validating if the screens follow the Komologorov theory was to utilize the work of Noll [23], where the turbulence is decomposed in a series of Zernike polynomials. Taking the first component of this series, it is derived that Δ_1, the variance of the mean-subtracted phase values in the phase screen within the telescope aperture should be related to the telescope diameter (D) and Fried parameters (r_O) according to the following equation:

$$\Delta_1 = 1.0299(D/r_o)^{5/3} \tag{3.4}$$

Generating a series of phase screens for several values of r_O, the value of Δ_1 calculated from the screens is compared with the analytical values calculated from Equation 3.4, with the results seen in Figure 3.5(a). While the calculated values for the screens do indeed follow a similar power law, they are scaled lower. This appears to be due to the outer scale factor in the AOTools library. For the set-up documented, a pixel screen of 512 width, with a telescope diameter of 8 metres, the maximum setting possible for L0, the outer scale factor, is 40 metres. Any setting above is not supported by the library. In Goncharov [24], a compensation factor for the variance reduction due to finite outer scale is derived. Applying this compensation to the values calculated from the screen, a good fit is found with the model, as can be seen in Figure 3.5(b). The outer scale may also be the cause of the lower than expected

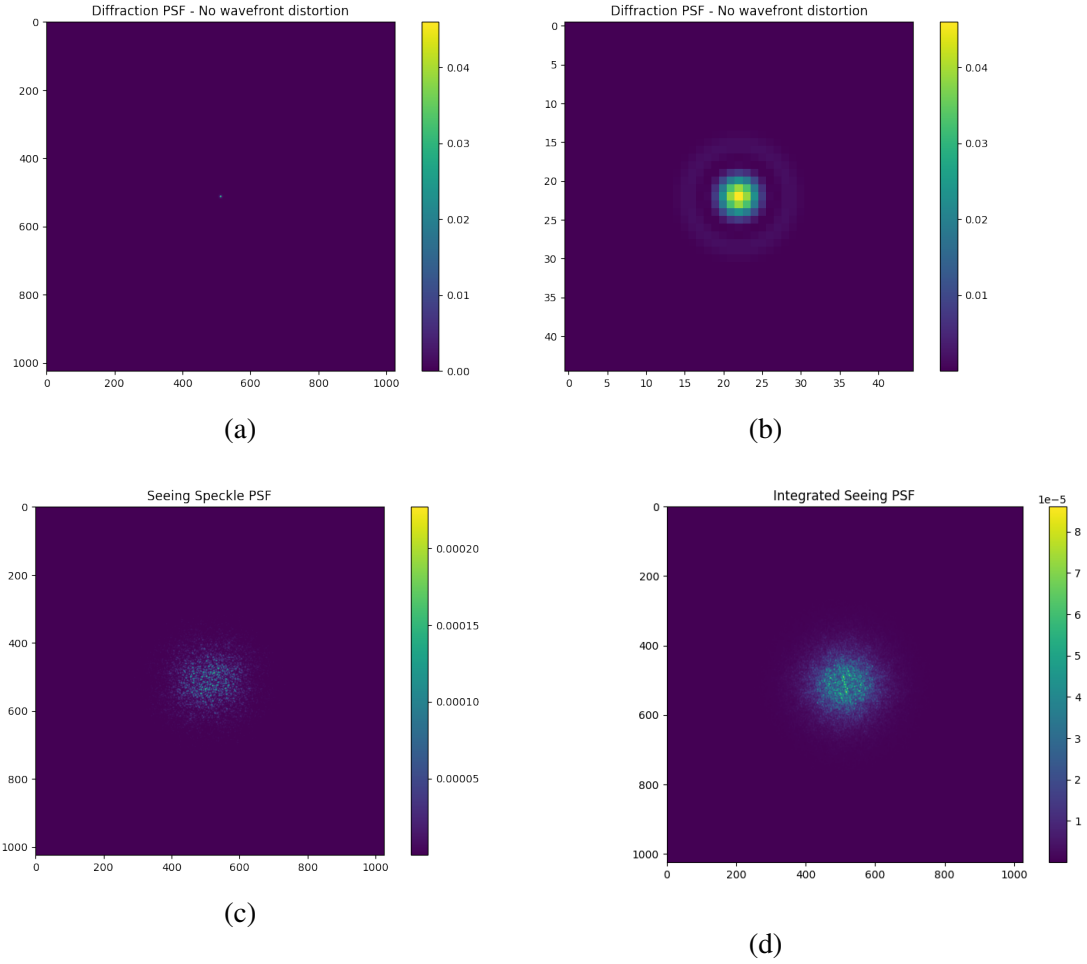

Figure 3.3: PSF functions produced by the Seeing simulation method described in the text. (a) Diffraction PSF showing a sharp PSF (b) Zooming into the Diffraction PSF, where the Airy pattern may be seen (c) Seeing PSF resulting from a single phase screen shown in Figure. 3.2. The speckle pattern is clearly seen, with a far greater spread than the diffraction PSF (d) Average Seeing PSF after integrating over 100 individual PSFs resulting from 100 phase screens, where the Seeing Disk can be seen emerging

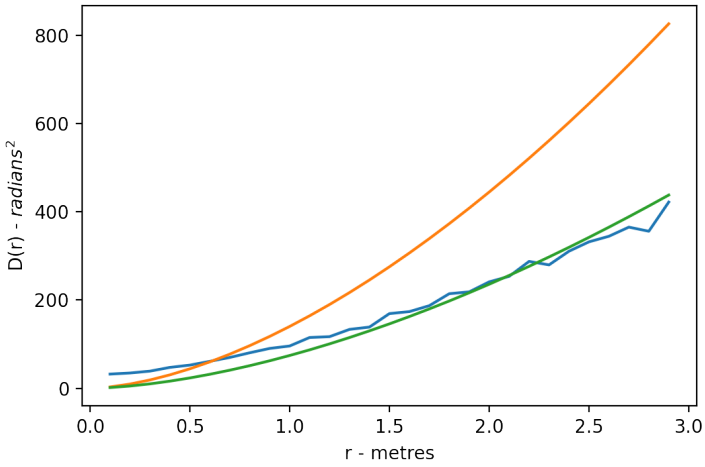

Figure 3.4: Estimates of structure function from AOTools generated phase screen (blue) where r_O=0.164m, and the theoretical values from Equation 3.3 for r_O=0.164m (orange) and r_O=0.24m (green). In order to calculate the estimates, 1000 screens were generated, and radial rings from the centers were used to estimate phase differences at different distances from the center.

structure function values in Figure 3.4.

A library was developed to enable the generation of input images using all the above techniques and the details may be found in Appendix A for further use.

3.2 EMCCD Simulation Process

The next stage of the simulator propagates the image plane photons through the EMCCD shift register. In the register, multiplicative gain through impact ionisation and clock-induced charge(CIC) were modelled. In order to model multiplicative gain, a Bernoulli trial using probability P_m was conducted for each electron entering a register in the shift register to see if a second electron is produced. This was repeated for the remaining $m - 1$ registers. To model the CIC process, an additional Bernoulli experiment using probability P_c was conducted for each of the m registers. Finally, when this simulated shift through the m registers is completed, Gaussian noise is added to the output value to model the readout noise process.

An example of a simulated Gaussian source input image and the resulting output image after being shifted through the EMCCD simulator is shown in Figure 3.6, along with the associated histograms.

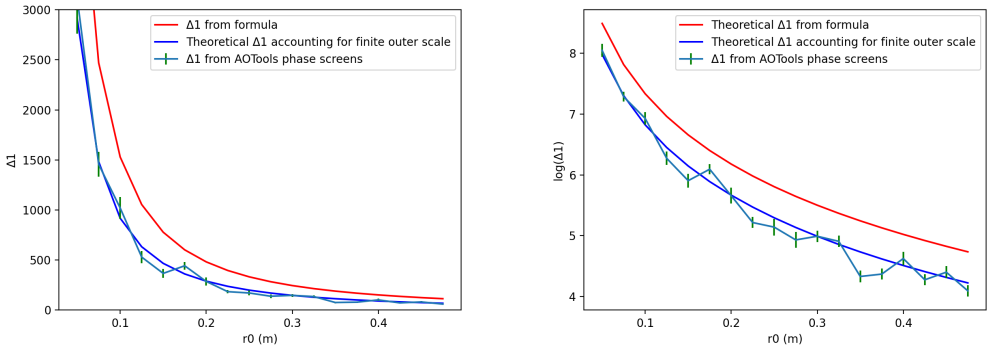

(a) (b)

Figure 3.5: (a) Values of Δ_1 in turquoise are from the simulated phase screens generated using AOTools for a variety of different r_O (Fried parameter) values, where D (telescope diameter) was 8 m and the screen sizes were 512x512. 100 different phase screens were used for each r_O value. In red are the theoretical Δ_1 values. In blue are theoretical Δ_1 values when taking into account the finite L_O outer scale value in the simulations (40 m) (b) Showing the same but with Log values

The EMCCD simulator code was developed in Python and may be found in the Appendix A. High gain significantly slows down the simulation process due the the large number of electrons that need to be simulated. As the simulation process is independent for each simulated input photo-electron, it is possible to parallelize the code so a large number of input photo electrons could be simulated. In theory this can scale as $O(n)$. However, as Python is not easy to parallelize to multiple threads that can run simultaneously due the Global Interpreter Lock (GIL) in the standard implementation, a version of the simulator code was also written using the Apache Spark framework, which allows horizontal scalability across threads, CPUs and even computers. This easily enabled on the order of millions of photo electrons to be simulated within several hours on an 8-core PC.

3.3 Validating methods using simulation

Using the source and EMCCD simulation, the calibration methods outlined previously may be validated. In particular, the histogram Slope, fitting EMCCD noise model parameters and Calibration-on-The-Spot (COTS) methods were tested through simulation.

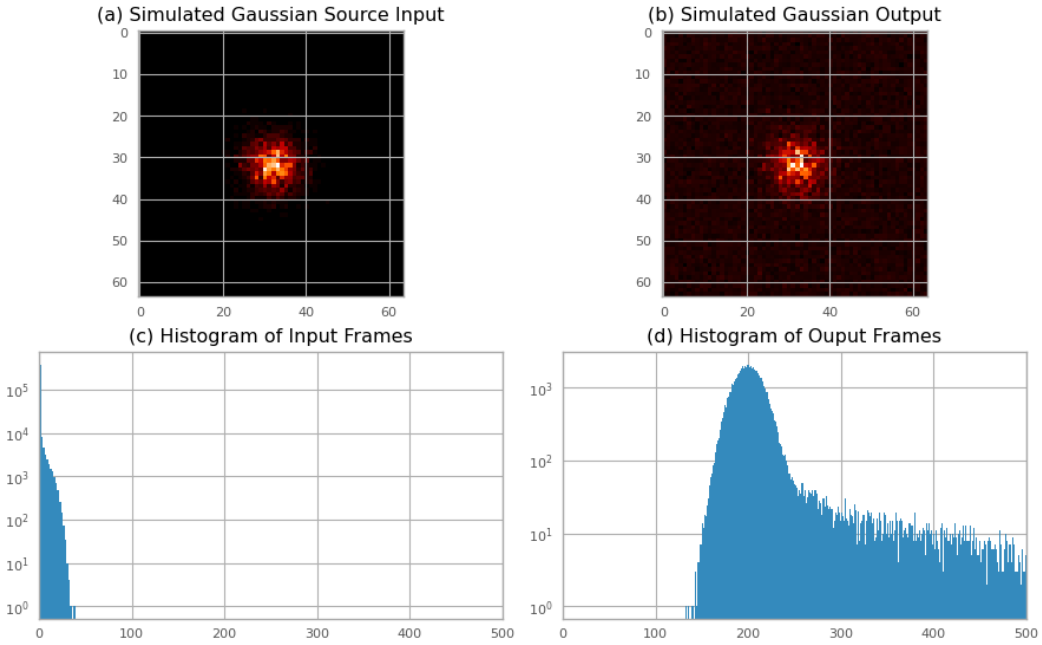

Figure 3.6: Examples from the simulation environment (a) A frame from the Poisson sampled Gaussian source (b) The simulated output frame after passing through the simulated EMCCD (c) The input histogram for several input frames (d) The output histogram for several frames after passing through the simulated EMCCD with a gain of 30. Both the readout noise and tail due to the EM register may be seen

.

Histogram Slope

To test and validate the general simulation set-up, initially a flat field input containing 1-photon per pixel was generated for 500K pixels and simulated through the EMCCD simulator. This is the ideal photon level for this method, where the log of the output histogram should contain a linear slope. The Histogram slope method was then applied to this output data to recover the gain. The fitting region started at the 5.5 σ offset, but a heuristic was chosen for selecting the outer fitting point, namely a fraction of the maximum end output value O_f. For the results shown in Figure 3.7 (a)(b), O_f was set to 0.7. The estimated gains match the nominal gains quite well, but there is a bias at higher gain level. The cause of this is not clear. It was suspected this might be due to numerical sensitivity due to low sampling at the higher output counts in the histogram. In order to investigate if this was the case, first the sampling was increased and second the fitting region were changed.

Increasing to pixel sample count 5 million pixels did not reduce the bias. In order

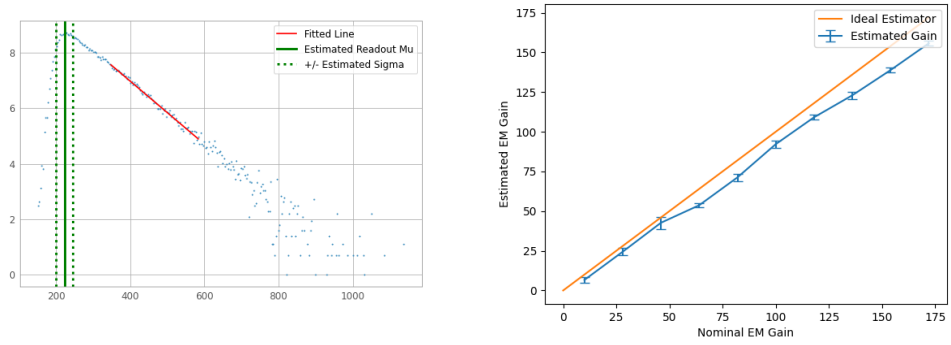

(a) (b)

Figure 3.7: (a) Histograms slope fits of output images of the flat field simulation (EM Gain = 100) and (b) the estimated EM gains versus nominal EM gains for a range of EM Gain values. For each simulation, 500k input pixels were simulated, the readout bias μ = 100 ADU and readout noise of σ = 10. Input is flat field of 500k input pixels each with exactly 1-photon

the investigate if the selection of the fitting region could improve the result, the outer and inner fitting points were modified.

A series of different end output value O_f were tried, with the results shown in Figure 3.8. After varying bias due to the small fitting range for low value, the bias reduces for larger values of O_f and does not appear to be significantly affected by fitting in the part of the histogram with low sample counts. So the source of the bias at higher EM gain values in the gain estimation of this method is not understood in the context of this simulation setup.

Next, a simulation was run that simulated some parallel clock induced charge (pCIC). In this case, the input pixels were Poisson sampled where $\lambda = [0.5, 1.0, 1.5]$, simulating increasing levels of pCIC. This is modelling a scenario where the source is faint at <1 photon per frame but pCIC causes some pixels to have more than 1-photon per frame when they enter the EM register. The results may be seen in Figure 3.9(a)(b)(c). The non-linear neck is due to the pCIC effect. The accuracy of the estimations for three different levels of pCIC may be seen in Figure 3.9(d).

In order to model the serial clock induced charge (sCIC), a simulation of this phenomenon was added to the EMCCD simulation run. The output may be seen in Figure 3.10(a)(b). In this run, sCIC was simulated with a P_c = 0.02, which is a typical value from the literature (for example ([20]), and P_c = 0.05 to show the

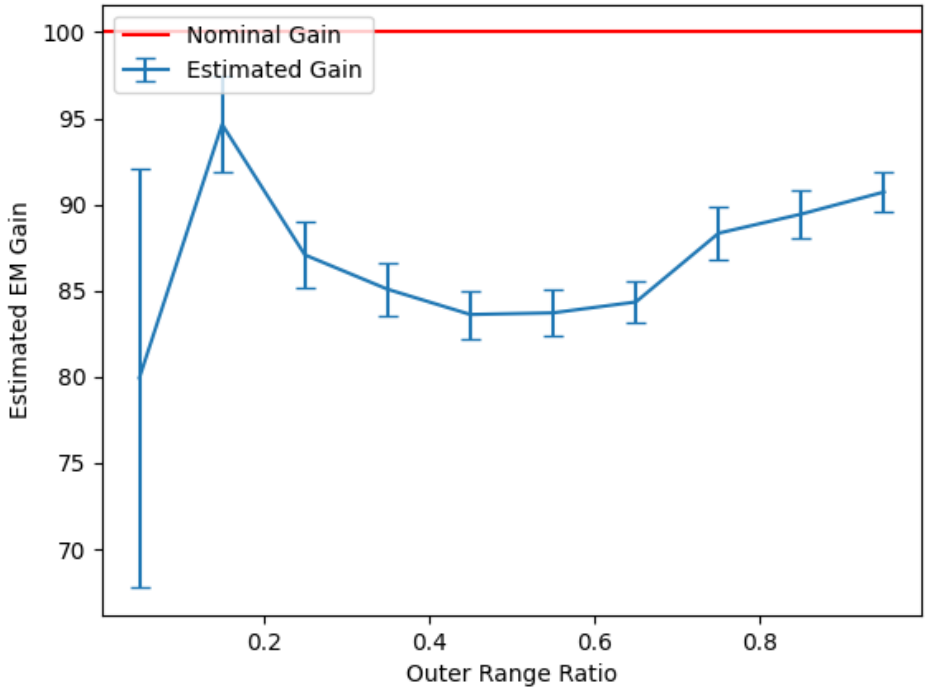

Figure 3.8: Estimated gains for a variety of end output values O_f for 500k input pixels, 1-photon input counts, EMCCD gain 100, the readout bias of μ = 100 ADU and readout noise of σ = 10

.

effect of elevation sCIC on the gain estimation, where P_c is the probability of a clock induced charge during each serial shift. A bias may clearly be seen in the estimates in Figure 3.10(c). Finally, the combined effects of pCIC and sCIC were simulated, and the results may be seen in Figure 3.11(a)(b)

The simulations show the histogram slope methods is relatively robust in the presence of some levels of sCIC and pCIC, once an appropriate fitting range is selected. While flat fields with less than 1-photon might be realistic for faint sources or very high speed frame rates, for point sources, the high flux rates near the center of the source, will heavily bias the estimation for the Histogram slope technique. This topic will be addressed further in Chapter 5.

Fitting EMCCD noise model parameters

The same set of flat-field simulations as in the previous section were undertaken again, but this time using the methods that fit the EMCCD noise model parameters to

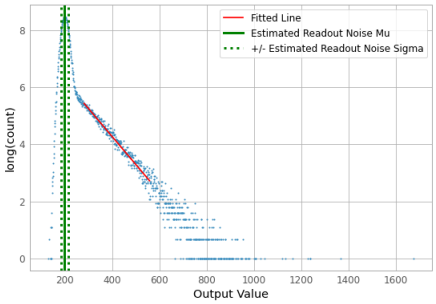

(a) pCIC (λ=0.5)

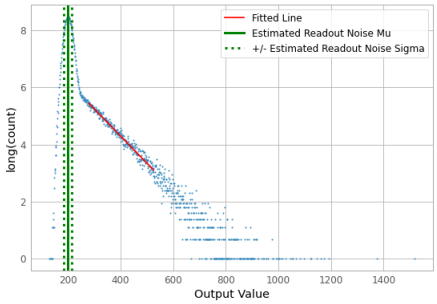

(b) pCIC (λ=1.0)

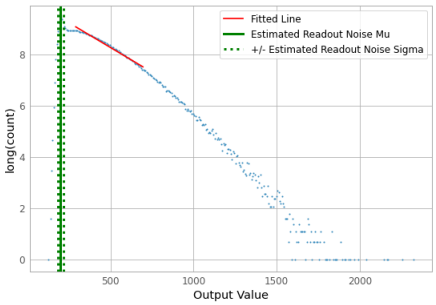

(c) pCIC (λ=1.5)

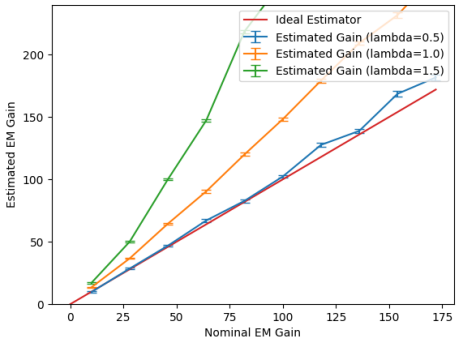

(d) Estimated vs Nominal, with different pCIC levels

Figure 3.9: (a)(b)(c) Histograms slope fits of output images of the flat field simulation (EM Gain = 100) for three different level of pCIC (d) Estimated EM gains versus nominal EM gains for a range of EM Gain values. For each simulation, 500k input pixels were simulated, the readout bias was μ = 100 ADU and readout noise σ = 10. Input is 500k with Poisson sampled values

the output data. Both the simple Gaussian-Exponential mixture model and the more complex mixture model that incorporates clock induced charge were simulated. The results may be seen in Figure 3.12 . Neither method suffers the bias at higher gains seen in the histogram slope method, and they both perform similarly given there is no clock induced charge in this initial simulation.

Next, clock induced charge was added to the simulation, both in the form of pCIC and sCIC as previously described.

For the simulation with pCIC only, seen in Figure 3.13 , the two model methods perform similarly to the histogram slope method. When pCIC and sCIC are both present, seen in Figure 3.14 , both methods are closer to the histogram slope method.

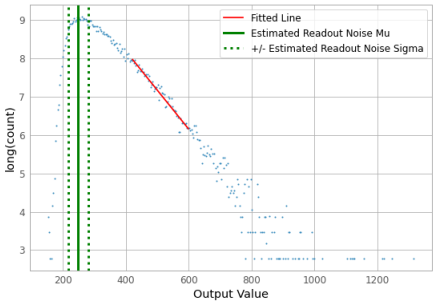

(a) sCIC, $P_c = 0.02$

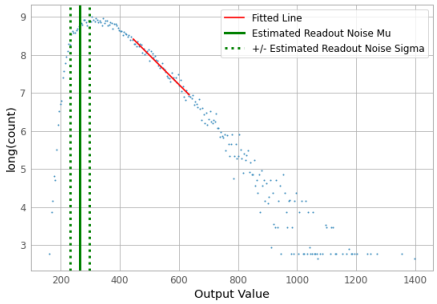

(b) sCIC, $P_c = 0.05$

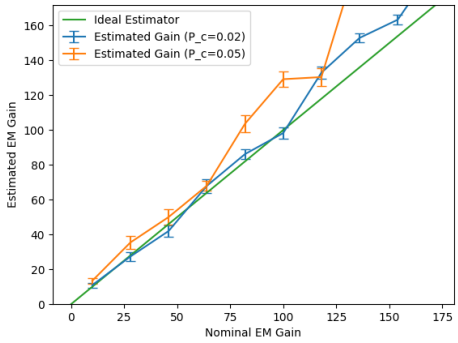

(c) Estimated versus nominal, different sCIC levels

Figure 3.10: (a)(b) Histograms slope fits of output images of the flat field simulation (EM Gain = 100) for two different levels of sCIC (b) Estimated EM gains versus nominal EM gains for a range of EM Gain values at different sCIC levels. For each simulation, 500k input pixels were simulated, the readout bias was $\mu = 100$ ADU and readout noise was $\sigma = 10$. Input is 500k pixels with 1 photon counts

In this latter scenario, which the more complex model attempts to model, it begins to out perform the simpler model.

Calibration-on-The-Spot (COTS)

The COTs alogorithm was also used to estimate the gain using the simulation setup. In this case, Gaussian and Moffat shaped sources were simulated. An example of an input and output image may be a seen in Figure 3.15 for a Gaussian source, along with the estimated gains. Accurate recovery of the gain is noted for a range of gain values. As mentioned in the description of the method, the individual estimates exhibit high variance, but when averaged over multiple single-frame estimates, this is reduced.

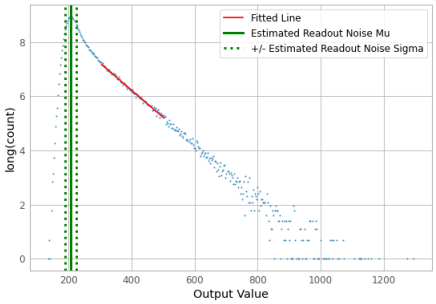

(a) sCIC, P_c = 0.02

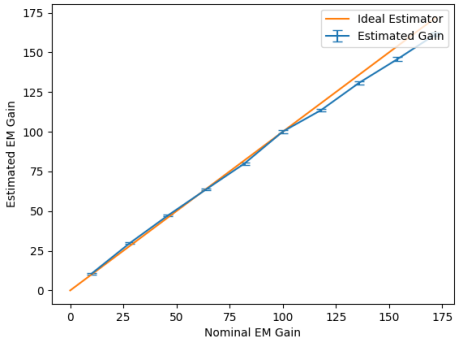

(b) Estimated versus nominal, with sCIC and pCIC levels

Figure 3.11: (a) Histogram slope fit of output images of the flat field simulation (EM Gain = 100) for with sCIC P_c = 0.05 and pCIC (λ=0.5) is present (b) Estimated EM gains versus nominal EM gains for a range of EM Gain values. For each simulation, 500k input pixels were simulated, the readout bias was μ = 100 ADU and readout noise was σ = 10. Input is 500k pixels with 1 photon counts

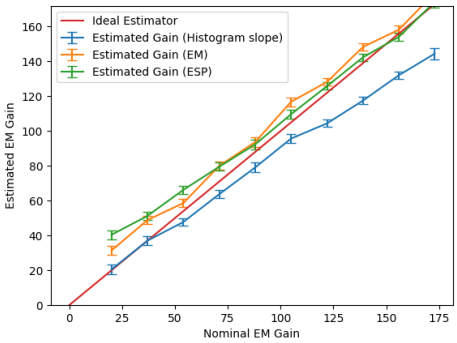

(a)

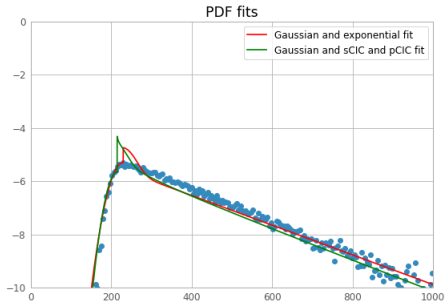

(b)

Figure 3.12: (a)Applying the noise model fit techniques for a variety of EM nominal gains. Both the simple and more complex models that incorporate clock-induced charges are shown. 500K pixel were simulated, 1-photon each, with no pCIC or sCIC simulated (b) The log of the PDF function of the resulting model fits for EM gain of 175, for the same simulation as in Figure 3.14

As the Moffat Distribution is a better approximation for a seeing disc of an astronomical source, the simulation was repeated with a Moffat shaped source. The result may be seen in Figure 3.16 , where a slight bias is seen. The most important

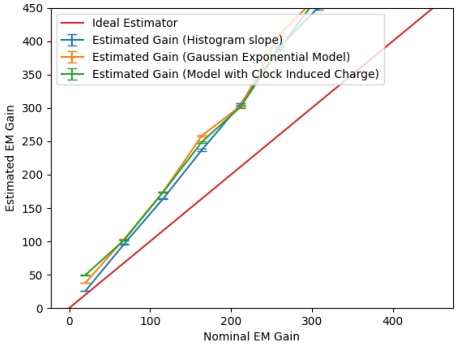

(a) pCIC, λ = 1.0

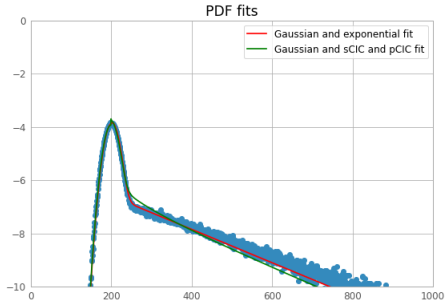

(b)

Figure 3.13: (a) Applying to model fit techniques for a variety of EM nominal gains. Both the simple and more complex model that incorporate clock-induced charge are shown. 500K pixel were simulated, 1-photon each, with input pCIC simulated with Poisson sampled values where λ=1.0 (b) The log of the PDF function of the resulting model fits for EM gain of 175

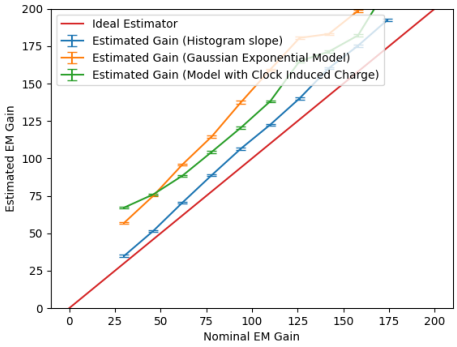

(a)

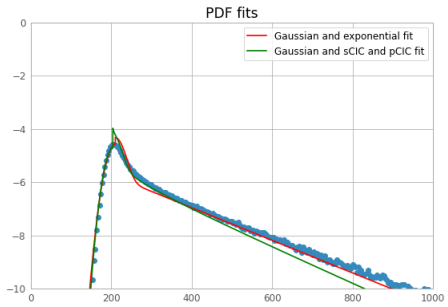

(b)

Figure 3.14: (a)Applying to model fit techniques for a variety of EM nominal gains. Both the simple and more complex model that incorporate clock-induced charge are shown. 500K pixel were simulated, 1-photon each, with input pCIC simulated with Poisson sampled values where lambda=0.5 and sCIC simulated where P_c = 0.02 (b) The log of the PDF function of the resulting model fits for EM gain of 175

parameter to make this method effective for this type of source was the amount of data used.

The simulation shown uses 7-pixel square area centred on the the source as data for the algorithm. Using data deep into the tails does cause a bias that over estimates gain

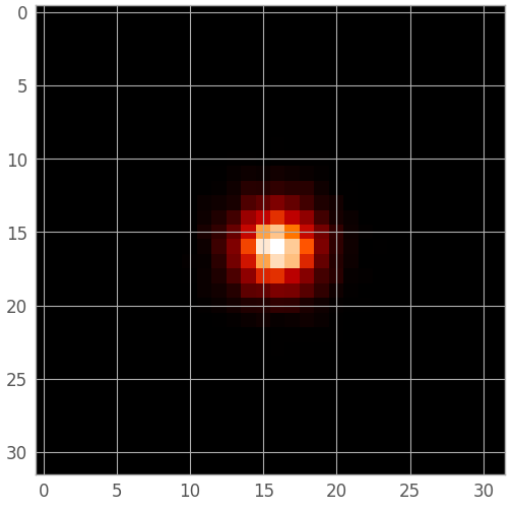

(a) Input Gaussian Source

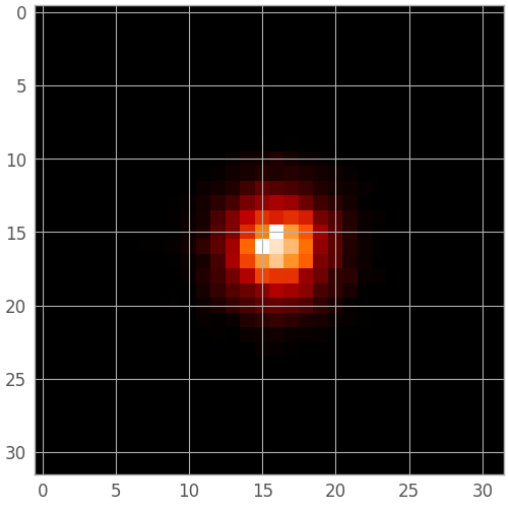

(b) Output Gaussian Source

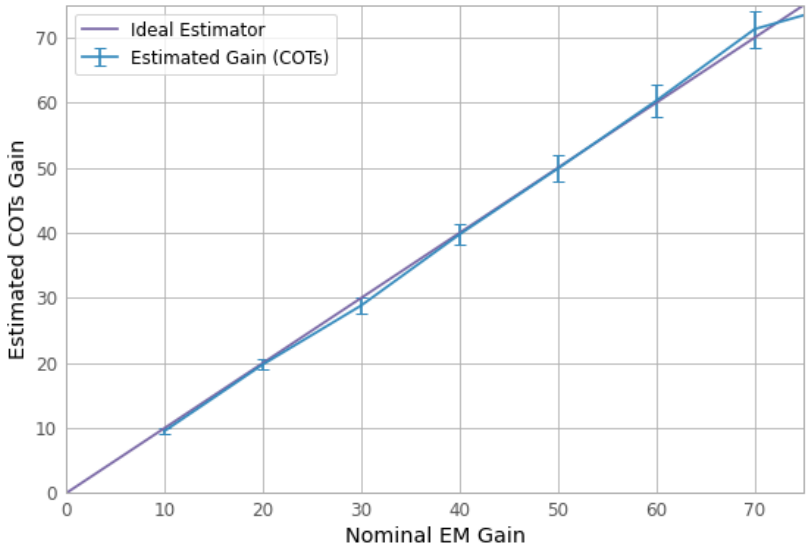

(c) Estimated gain using COTS method for Gaussian source

Figure 3.15: (a) Input Gaussian Source σ = 2.4 (b) Output Data after passing through EMCCD simulator with EM Gain = 50 (c) Estimated gains using COTS method for a range of gain values, averaged over 50 frames

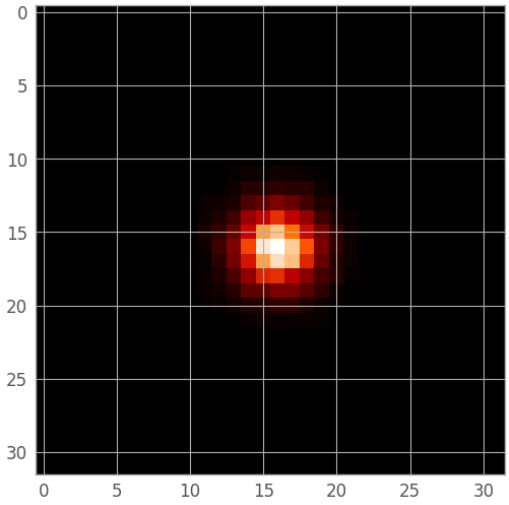

(a) Input Moffat Source

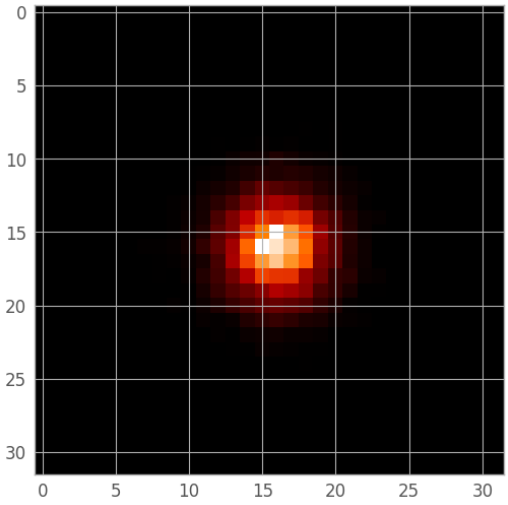

(b) Output Image

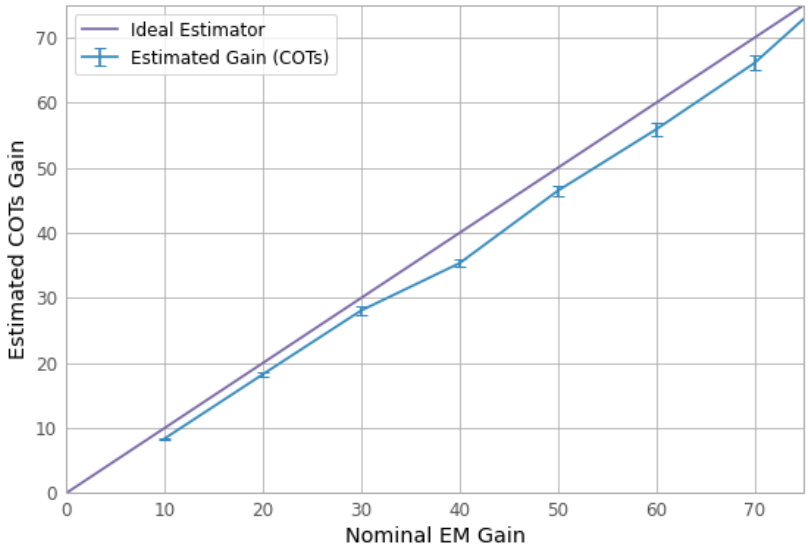

(c) Estimated gain using COTS method for Moffat Source

Figure 3.16: (a) Input Moffat Source where $\alpha = 4, \beta = 4$(b) Output Data after passing through EMCCD simulator with EM Gain = 50 (c) Estimated gains using COTS method for a range of gain values, averaged over 50 individual frame estimates

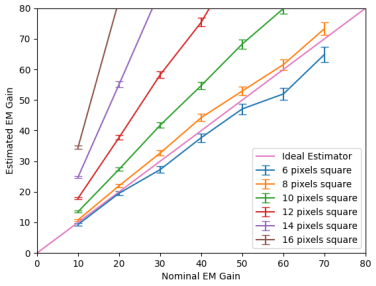

(a) Varying pixel areas

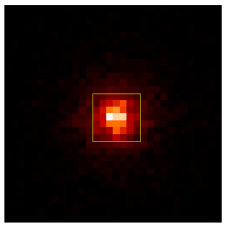

(b) Optimal pixel area

Figure 3.17: (a) Estimated gains for different pixel areas used (b) 7-pixel box

to occur, so in applying this techniques without adopting a Moffat-fitting algorithm might require staying away form the tails using a suitable heuristic. Some increasing pixel areas and their associated bias may be seen in Figure 3.17.

The next step was to understand how astronomical seeing would potentially affect this technique. Using the speckle generation technique previously described, input speckle images were generated. The results of these parameters on the gain estimation may be seen in Figure 3.18 (a). Accurate gain estimation may be achieved with sufficient integration and photon rate. Another advantage of this technique is that it should be insensitive to CIC. In order to understand how the presence of clocked induced charge affects the accuracy of this estimation technique, similar amounts of serial CIC were injected into the simulation as in the previous section ($P_c = 0.05$), and it can be seen to not bias the estimation. Parallel CIC was not simulated, as this would be dwarfed by the high photon counts present in the point source input images.

In order for the techniques to produce the accurate results in simulation, a certain threshold of integration, photon level and binning were required. Figure 3.19 show to impact of insufficient integration or flux levels on the gain estimation.

Summary and comparison of Simulation results

Several of the methods were tried in a simulation environment, with different amounts of gain and clock-induced-charge effects, to understand their performance better in different scenarios.

Simulating faint sources, it was found the histogram slope method could recover the gain in the presence of some levels of sCIC and pCIC, once an appropriate fitting

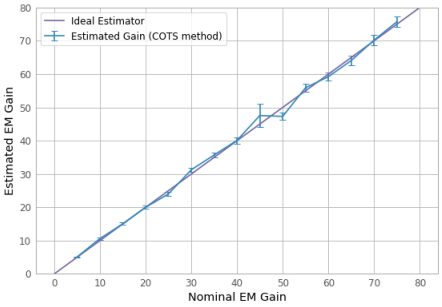

(a) Estimated EM using COTs for simulated seeing limited source

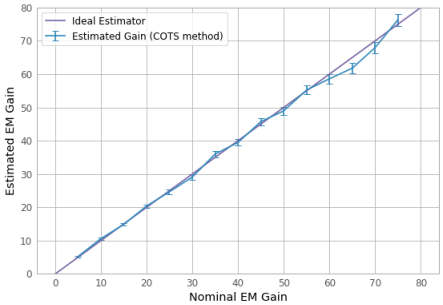

(b) with serial clock induced charge

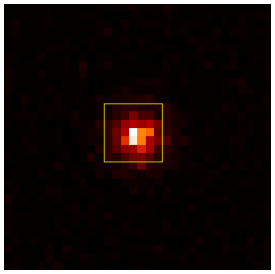

(c) Sample output frame of seeing limited source integrated for 50 frames

Figure 3.18: (a) Estimated gains using COTS for a variety EM gains, for a simulated seeing input source (b) Same simulation with the presence of high serial clock induced charge ($P_c = 0.05$) (c) Sample output frame of seeing source simulated. Source simulation parameter were: Screen size = 256, D (telescope diameter) = 8 metres, r_0 (Fried Parameter) = 0.2 metres, L0 (Outer scale) = 100 metres, wavelength = 500 nanometres, integration = 100 frames, peak flux rate = 2000 photons

range was selected. There was a bias at higher gains, but the cause could not be determined.

The EMCCD noise model parameters method performed comparably for faint sources, once the gain was sufficiently high for the mixture-model approximations to be valid, with the more complex model outperforming the simpler model when both pCIC and sCIC were simulated.

While simulating a seeing limited source, it was shown the COTs method could recover the gain when sufficiently high photon rate and integration level. Is was also shown using a 2-D Gaussian approximation was sufficient for the PSF model in this

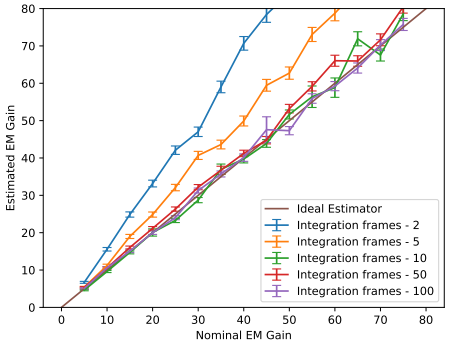

(a) Increasing integration levels

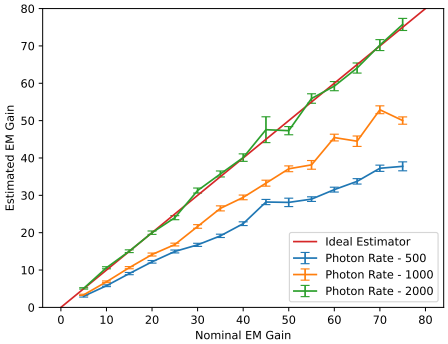

(b) Increasing flux levels

Figure 3.19: (a) EM Gain estimates when integration is varied (b)EM Gain estimates when the per frame photon count is varied

scenario, as only the inner core needs to be used for the estimation.

Chapter 4

Laboratory Results

In order to further test the gain calibration methods, data was collected in a laboratory setting using EMCCD detectors. This would allow some of the standard gain calibration techniques to be explored, and values derived of nominal versus estimated gains could be compared to results from the astronomical estimation results.

4.1 Laboratory Set-up

An iXon Ultra 897 EMCCD camera manufactured by Andor was set-up in the laboratory along with a light source. This camera, which is one of the two cameras taken from the same GASP instrument [15] set-up described in Chapter 5, has a 512x512 pixel array, and can achieve overall gains of up to 1000x according to the manufacturer.

A Thorlabs stabilised light source, the SLS201L/M, was employed. In this device a tungsten-halogen bulb provides constant intensity blackbody radiation over a wavelength range 360-2600 nm. Internal feedback is used to stabilise the output to 0.01% per hour, and 0.1% per $^{\circ}C$. The source included a variable Dovetail attenuator to adjust the light output level. A piece of white perspex was placed between the source and detector to scatter the light and remove any structure in the beam i.e. producing a flat field.

4.2 Details of Data Collection

Several different data sets were collected in the laboratory in order to be used with the different methods. All datasets were collected with the same detector and set-up described above.

(a) Increasing Exposure Series: A dataset recorded where the light source intensity remained constant, but the exposure time was increased for each frame recorded by the EMCCD detector. The data was collected for three different nominal EM gain level set-points, [0, 20, 30], with both dark and flat fields recorded. Each series consisted of 80 frames, with the exposure time increasing from one frame to the next, resulting in each series having 1 sample of

data for each recorded intensity level. The purpose of collecting darks for both this and the subsequent datasets is to be able to subtract the darks from the flat fields, so that the bias does not have an impact on the Mean Variance technique. The purpose of the 0 EM gain dataset is to be able to determine the ADU factor.

(b) Discrete Intensity Series: A dataset where the total source flux for each frame was set at one of four discrete levels[1]. This was achieved by keeping the frame exposure time fixed, but using using different attenuator settings. Dark and flat data was collected for the same three nominal EM gain set-points of [0, 20, 30], like the previous data set. For each intensity level, 80 frames were recorded, this time resulting in 80 samples for each intensity level.

(c) Discrete Gain Series: A dataset where the source intensity level remained fixed, but the nominal EM gain was varied across gain set-points of [0, 20, 30, 50, 100, 500, 1000] where at each set-point, dark and flat data was collected. For each gain set-point 80 frames were collected.

4.3 Results

The standard Mean Variance (MV) technique was applied to the (a) varying exposure and (b) discrete intensity series datasets. The MLE intensity series (MLE IS) technique was additionally applied to the (b) discrete intensity dataset. Finally, the MLE gain series (MLE GS) technique was applied to the (c) discrete gain series. Due to both the computational complexity of the MLE methods with the associated algorithm run-time, and the fact that the center of the recorded laboratory images appears flatter than the extremities, only the central 40x40 array of pixels were used in calculating the results presented in this chapter.

Mean-Variance (MV) Technique

The MV technique was applied to both datasets (a, b) described in the section above.

(a) Increasing Exposure Series Data Set

Scatter plots for the Mean-Variance relationships at the 3 nominal EM gain levels are presented in Figure 4.1(a), where the relationship between variance and mean signal appears to be linear as the exposure time increases for the frames. Upon

[1]For the EM gain=30 series, an additional 3 intensity levels were used. Additionally one of the intensity levels recorded for EM gain=20 series had to be discarded due to files getting corrupted

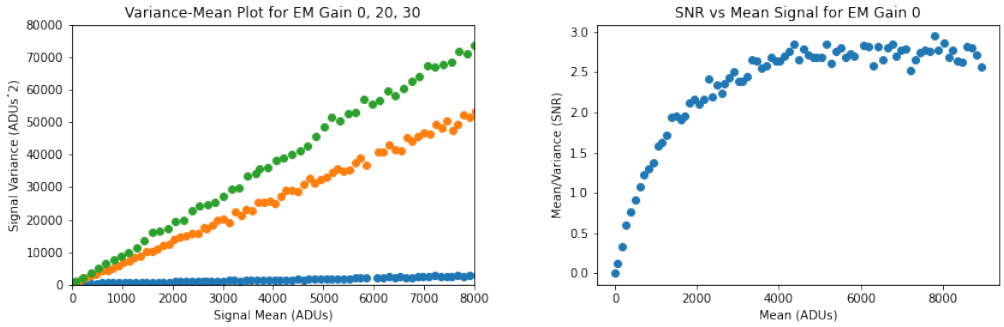

(a) (b)

Figure 4.1: (a) Mean-Variance plots for the increasing exposure series dataset for Nominal EM gains of 0 (blue), 20 (orange) and and 30 (green) (b) SNR versus mean Signal. It can be seen that the photon shot noise does not dominate until a certain threshold.

further examination of the signal to noise ratio (SNR, defined as the mean/variance here) versus mean signal in Figure 4.1(b), it can be seen that the photon shot noise does not dominate until a certain threshold is reached. Before this point the readout noise dominates, as mentioned in McLean [3]. Similarly at high intensities, the device will saturate, resulting in another non-linearity in the photon transfer curve, although the level of flux was not sufficiently large in this dataset for that to occur.

Because of the non-linearity, least squares fitting was applied after the non-linearity was excluded, using Figure 4.1b to determine a suitable cut-off point. The resulting least-squares fitted lines may be seen in Figure 4.2 for the three different nominal gain levels. First, equation (2.14) is used to provide an estimate for the ADU factor using the data when the EM gain was turned off. This estimated value was then utilised along with the recovered slope for the data with the EM gain turned on to estimate the EM gain using equation (2.15). The results of these calculations may be seen in Table 4.1.

Nominal EM Gain	**Fitted Slope**	**ADU Factor Estimate**	**EM Gain Estimate**
0	0.275	3.635	N/A
20	6.476	N/A	11.773
30	9.200	N/A	16.724

Table 4.1: Estimated Gain for increasing exposure series data set using MV Method

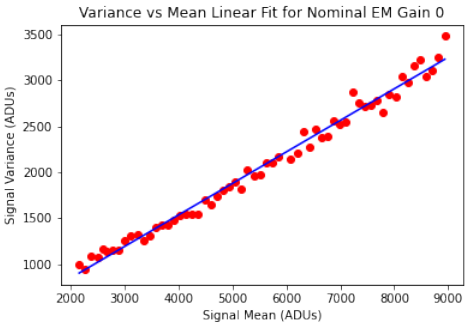

(a) Nominal EM Gain = 0

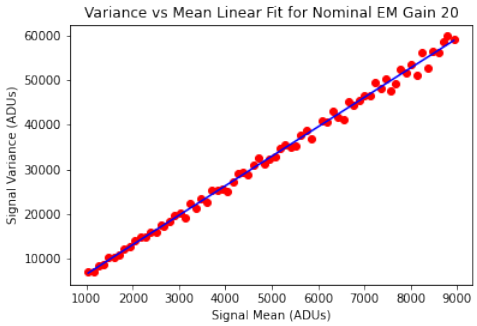

(b) Nominal EM Gain = 20

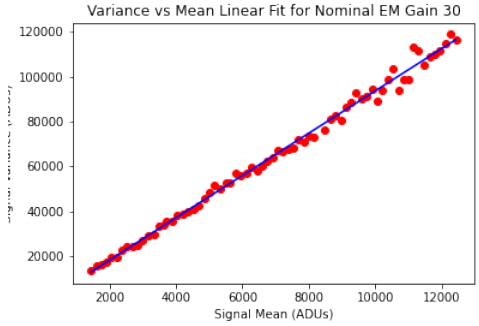

(c) Nominal EM Gain = 30

Figure 4.2: Increasing exposure data set least-squares fitted lines for the set of nominal EM Gains

(b) Discrete Intensity Series Data Set

The Mean Variance Technique was also applied to the discrete intensity series data set. The different discrete intensity levels can clearly be seen in the scatter plots in Figure 4.3 as separate clusters, where the mean and variance is calculated for each pixel across the 80 frames in the sequence. Firstly, a least squares line fit using all the data points was undertaken, shown by the blue lines in Figure 4.3 and the ADU factor and EM Gains were estimated, using the same method described in the previous section. The results may be found in Table 4.2.

Nominal EM Gain	Fitted Slope	Standard Error Slope	ADU Factor estimate	EM Gain estimate	EM Gain error
0	0.215	0.0029	4.633	N/A	N/A
20	5.954	0.0407	N/A	13.795	0.0942
30	9.330	0.0200	N/A	21.617	0.0463

Table 4.2: Estimated Gain for Discrete Intensity Series using MV Method

Ryan [14] also used the MV method to estimate gain from a discrete intensity series,

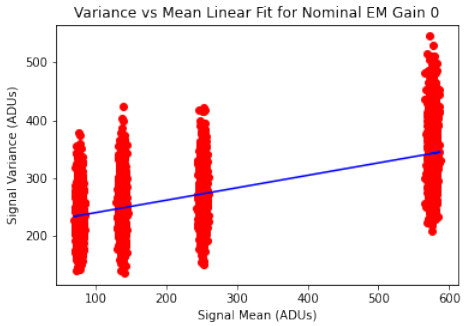

(a) Nominal EM Gain = 0

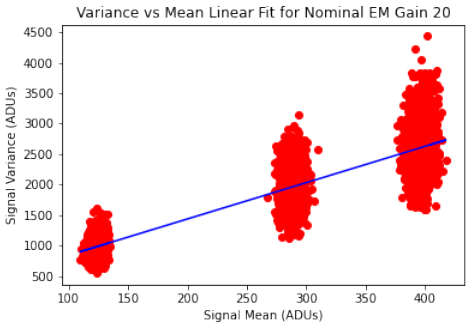

(b) Nominal EM Gain = 20

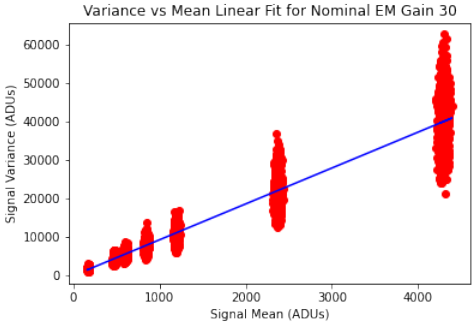

(c) Nominal EM Gain = 30

Figure 4.3: Mean-Variance plot for the discrete intensity series dataset for each of the nominal gains. Least-square line fits are shown in blue

but instead of using all the data for a single line fit, the author obtained line fits for each pixel and in turn gain estimates for each pixel. Then they used the mode of the resulting distribution of pixel level estimates to obtain a gain estimate.

This method of calculating per-pixel estimates was applied to this data set, using a square of 1600 pixels around the center. The resulting distributions of ADU and EM Gain estimates may be found in Figure 4.5. Retrieving the mode of these distributions, the estimates using his per-pixel MV technique may be found in Table 4.3

Nominal EM Gain	**ADU Factor Estimate**	**EM Gain Estimate**
0	3.260	N/A
20	N/A	9.566
30	N/A	14.684

Table 4.3: Estimated Gain for Discrete Intensity Series using MV Method (per pixel)

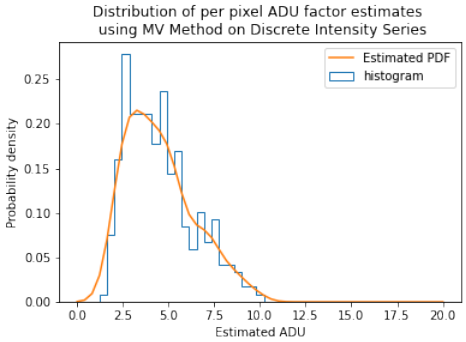

(a) Nominal EM Gain = 0

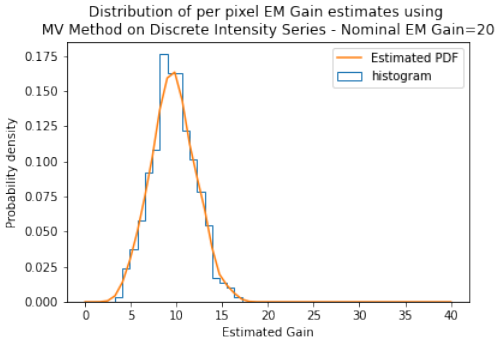

(b) Nominal EM Gain = 20

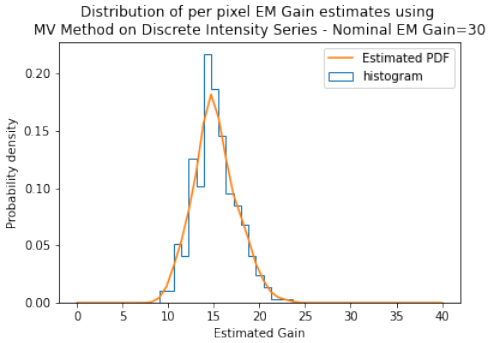

(c) Nominal EM Gain = 30

Figure 4.4: Distribution of per-pixel estimate using MV method for the ADU factor and EM Gain for the discrete intensity dataset for the set of nominal gains

Maximum Likelihood Estimation Intensity Series Method (MLE IS)

Due the complexity of the algorithm, the Python code library developed by Ryan [14] found at [25] was used. This algorithm is particularly computationally intensive compared to the previous MV methods, with much longer running times, taking several hours to run on a 4-core desktop computer for the 40x40 pixel area outlined previously.

To use the MLE algorithm on both the intensity series and gain series for EM gain estimation, the ADU factor must be estimated first using the Intensity Series MLE algorithm. This is done using the intensity series data with the EM gain turned off. The MLE algorithm is used, and the results for the 1600 pixels are shown in Figure 4.5(a). The resulting estimate, the mode of the distribution, is very close the nominal value of 4 given by the manufacturer.

Once the ADU value is estimated, it can be be used in the MLE Intensity Series algorithm to calculate the EM Gain. Once again, individual estimates were computed at a pixel level, and may be found in Figure 4.5(b). The resulting estimates can be

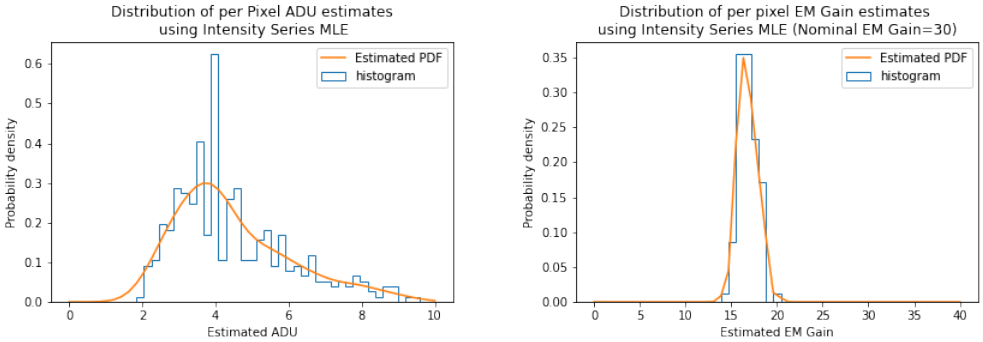

(a) (b)

Figure 4.5: (a) Results from estimating the ADU factor for 1600 pixels using the IS MLE method. The fitted PDF from the histogram of per-pixel estimated is plotted. (b) Results from estimating the EM Gain for 1600 pixels using the MLE IS method, where the nominal gain was 30. The fitted PDF from the histogram of per-pixel estimates is plotted

Nominal EM Gain	**ADU Factor Estimate**	**EM Gain Estimate**
0	3.7387	N/A
20	N/A	10.8768
30	N/A	16.4320

Table 4.4: Estimated Gain for Discrete Intensity Series using MLE IS Method

found in Table 4.4

Maximum Likelihood Estimation Intensity Series Method (MLE GS)

The MLE Gain Series algorithm was applied to the gain series data. This provided estimates of the EM Gain for each of the gain points in the series. The ADU estimate from the IS MLE is used as an input here, as the ADU factor may not be estimated from gain series data. Again, per-pixel estimates were computed for each pixel, and the distribution of these resulting gain estimates are shown in Figure 4.6 for the second set-point, which had a nominal gain of 30, with the results for all the gain point common to the previous series in Table 4.5

In order to see if the relationship between nominal and estimated gain remains consistent into high EM gains, the comparison of all the nominal gain set points and their estimates values can be seen in Figure 4.7, and in Table 4.6

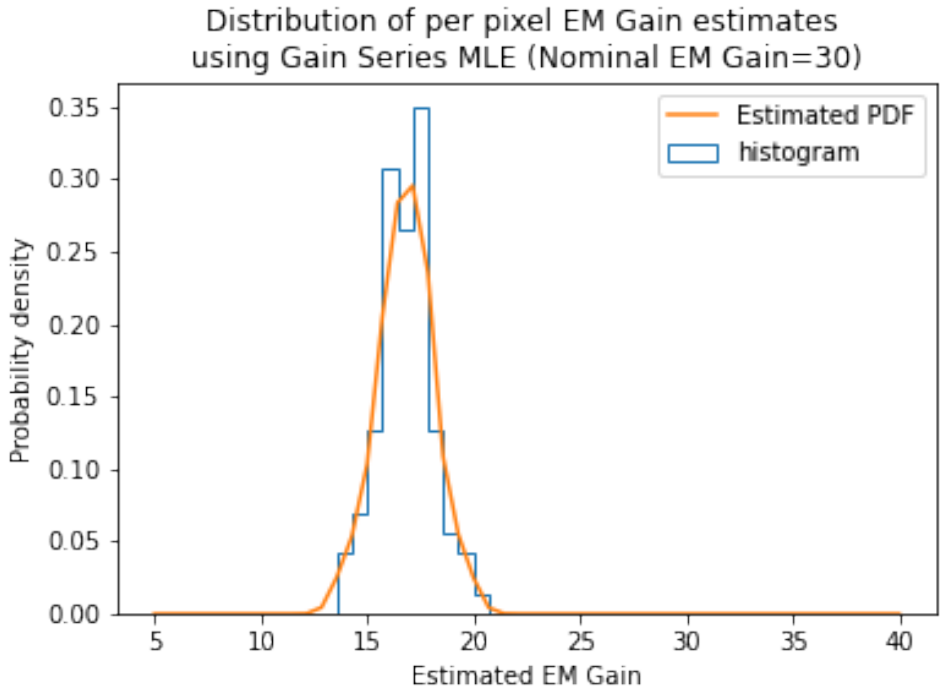

Figure 4.6: Results from estimating the EM Gain for 400 pixels using the MLE Gain Series method, showing estimates when the nominal gain was 30. The fitted PDF from the histogram of per-pixel estimated is plotted

.

Nominal EM Gain	**ADU Factor Estimate**	**EM Gain Estimate**
0	3.7387	N/A
20	N/A	12.0795
30	N/A	17.0550

Table 4.5: Estimated Gain for Discrete Gain Series using MLE GS Method

Nominal EM Gain	**EM Gain Estimate**
20	12.0795
30	17.0550
50	26.9023
100	50.0388
500	222.7485

Table 4.6: Gain series dataset nominal EM gain and EM gain estimates using MLE Gain Series Algorithm

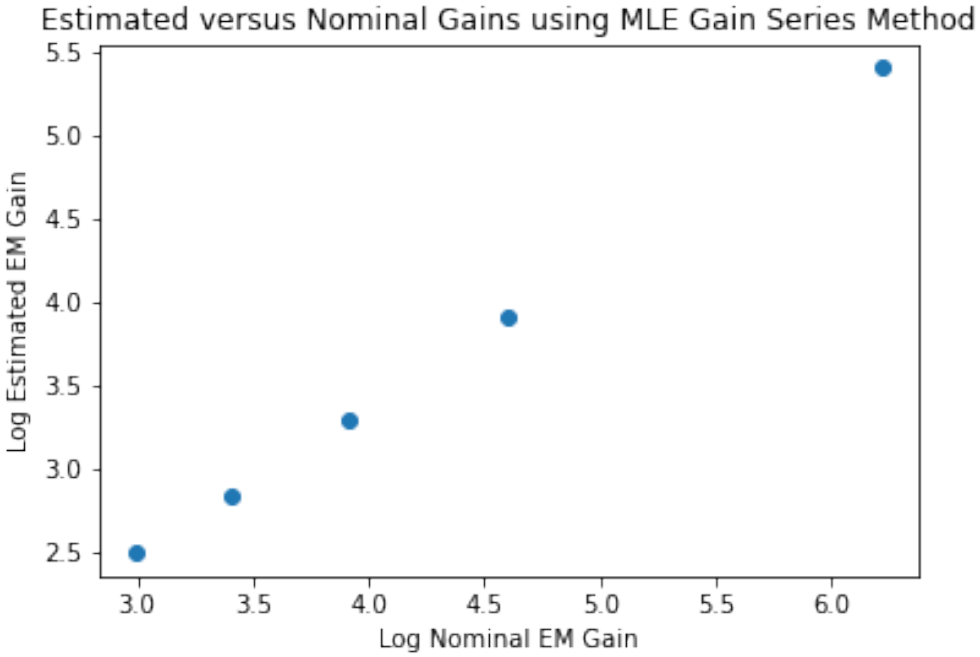

Figure 4.7: Comparing the estimate EM Gains with their corresponding Nominal values for all the gain set points in the series.

.

Summary and comparison of Laboratory results

The three methods (MV, MLE IS and MLE GS) delivered broadly similar and consistent results. A summary of the estimates may be found in Table 4.7. Using the MV approach on the discrete intensity series with an overall linear fit is a notable outlier, but when the per-pixel fits are done, it's estimates are in line with the other techniques. In all cases, the estimated EM gain values were significantly lower than the nominal values set on the detector, corresponding to approximately half the expected gain. Data was also collected on a second detector to ensure the particular detector was not defective, but similar results were found.

As the relative values between the different gain values shows a linear trend versus the nominal values, this indicates these methods would be useful for calculating the relative gain (the relevance of this is detailed in the next chapter), even if the true gain levels are not correct or at least inconsistent with the manufacturer's nominal gain.

Method	Data set	ADU Estimate	Nominal EM Gain 20	Nominal EM Gain 30
MV	Increasing Exposure Series	3.635	11.773	16.724
MV	Discrete Intensity Series	4.633	13.795	21.617
MV (per-pixel)	Discrete Intensity Series	3.260	9.566	14.684
MLE IS	Discrete Intensity Series	3.739	10.877	16.432
MLE GS	Discrete Gain Series	3.739	12.080	17.055

Table 4.7: Summary of calibration estimates for the different lab methods

Chapter 5

Astronomical Observation Results with GASP

5.1 GASP Instrument Details

Some of the techniques in the previous sections were applied to data obtained using the Galway Astronomical Stokes Polarimeter (GASP) at the 8 m Gemini South telescope. During this observation series, a variety of data was collected. This included data from standard sources, along with high speed data from the Crab Nebula. The standard sources were observed as they had previously measured polarisation that could be compared to the result obtained using GASP to validate the calibration of the instrument.

Details of the GASP instrument are presented in O'Connor [15], where the hardware is described along with how the instrument measures the four components of the Stokes vector simultaneously. The GASP instrument uses two Andor iXon 897 Ultra EMCCDs as the imaging detectors and enables full-FOV slow speed imaging at a frame rate of 56 frames per second (fps), and also limited FOV high speed imaging (>1000 fps).

Within the instrument (illustrated in Figure 5.1), the beam at the telescope focus is first collimated to a suitable pupil size, producing the main optical path S, which is then split at a prism face to give two optical paths: R-path - reflected, and T-path - transmitted. Both optical paths R-path and T-path are individually divided into two optical paths *rpath_1* and *rpath_2*, and *tpath_1* and *tpath_2*, respectively, by a Wollaston prism on each of the paths. The Stokes vector can then be determined from the intensities of the 4 different paths, using a transformation described in O'Connor [15]. The instrument uses one EMCCD detector for the R-path, and another for the T-path. Due to the fact that the individual detectors may have different effective gains, an important part of the calibration procedure is to estimate the gain ratio $Gs_{T/R}$ between the two detectors, as this is used to compensate the intensities of the two channels before recovering the Stokes vector. This is given by:

$$Gs_{T/R} = \frac{Gs_{rpath}}{Gs_{tpath}} \tag{5.1}$$

where Gs_{tpath} is the system gain of the T-Path detector, and $Gs_{rpath}$is the system gain of the R-Path detector.

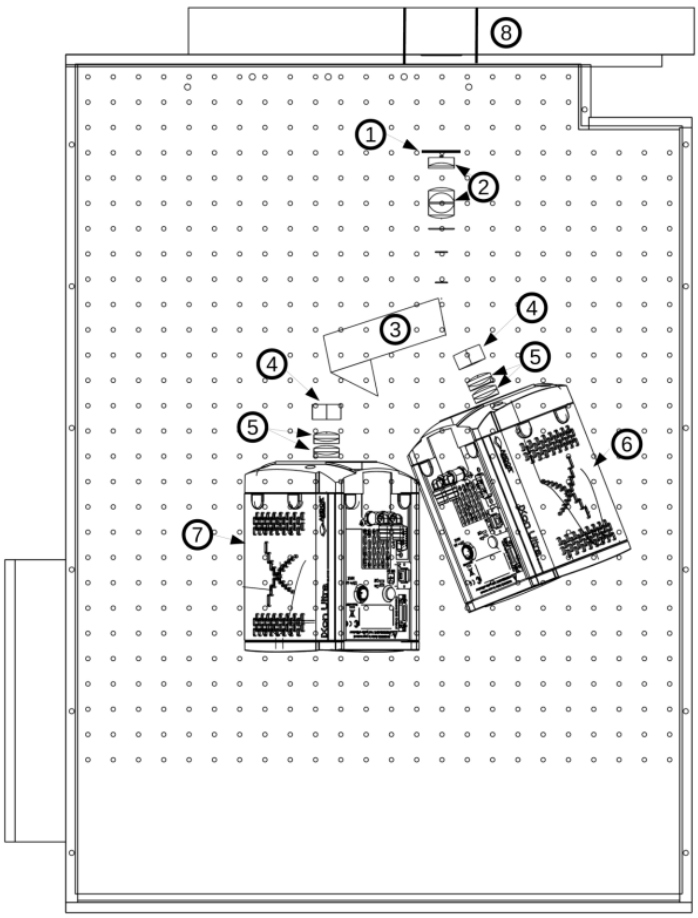

Figure 5.1: The GASP instrument from a top-down view (image sourced from O'Connor [15]). The main optical and detector components are numbered: 1. Optical Mask and Field Stop at the telescope focal plane. 2. Collimating Lens Assembly. 3. Retarding Beamsplitting Prism. 4. Wollaston Prism. 5. Re-Imaging Lenses. Camera. 6. Reflection Path Camera (R-path). 7. Transmisson Path Camera (T-path) 8. Flange Adapter Plate

5.2 Observation Details

Observations were taken using the GASP instrument at the 8 m Gemini South telescope in February 2019. Both the Crab Pulsar and several polarisation standards sources were observed.

5.3 Standard source results

The polarisation standard GSC 08169-00417 was recorded for 100 frames at a nominal gain of 200. An example of the output images for each of the 4 channels described above may be seen in Figure 5.2.

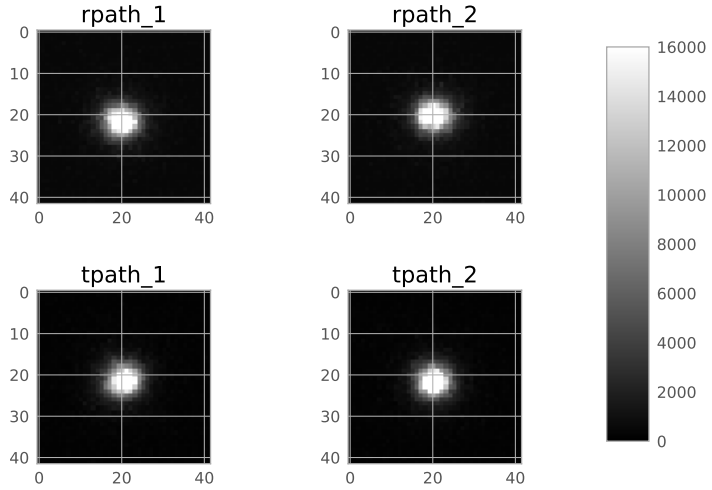

Figure 5.2: Output images from GASP instrument for 1-frame from the observation sequence of GSC 08169-00417

Histogram Slope

The Histogram slope method was applied to the standard source data. In order to apply this method, it is necessary to find which part of the output data corresponds to faint pixels that had less that one input photon per frame, in order for the exponential slope assumption to be valid. One approach is to select an annular region around the source in the output images as a basis for constructing the histogram. In order to select the correct annulus, we need to estimate a minimum radius where the single photon assumption should hold true. By starting with a reasonable estimate $\gamma_{nominal}$ for the nominal gain of the EMCCD, we can obtain the estimated peak number of photons at the centre of the source. The peak number of photons, N_{peak} is given

by:

$$N_{peak} = output_{peak}/\gamma_{nominal} \tag{5.2}$$

The $output_{peak}$ should be averaged over several frames given the stochastic nature of the output peak value. If we can then make an assumption on the PSF of the source, we can fit the image to a PSF model, and use the parameters of the model combined with the N_{peak} value to estimate the radius R outside which there is less than 1-photon per pixel per frame. For a source modelled as a Gaussian this is given by:

$$R = \sqrt{2(logN_{peak})}\sigma \tag{5.3}$$

where σ is the estimated variance of the PSF from a 2-D Gaussian fit. For a Moffat PSF, the formula is:

$$R = \alpha\sqrt{N_{peak}^{(1/\beta)-1}} \tag{5.4}$$

where α and β are the parameters of the Moffat distribution

This approach was applied to the data. Figure 5.3 shows fitted Moffat and Gaussian PDFs versus a cross section of pixel data. It can be clearly seen that the Moffat PDF fits the tails of the data more closely. Using the equations above, the optimal inner annulus radii were 9.23 pixels for Gaussian fit, and 19.86 pixels for the Moffat fit.

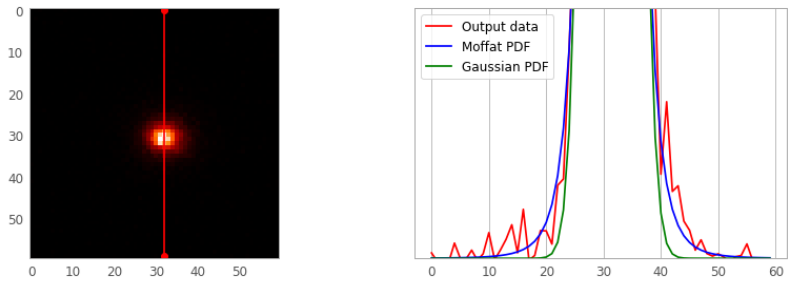

Figure 5.3: Left is example output input, with red line indicating cross-section show on right. Right is a plot the fitted Gaussian and Moffat PDF fitted against the output data for a data cross section

In order to see if these estimated optimal radii were a reasonable starting point for the inner annulus radius to use, the gain was estimated using the histogram fit method for a variety of inner annulus radii, whilst keeping the outer radius constant, with the result seen in Figure 5.4. For flux of greater that 1-photon per pixel, it would be

expected that the gain would be overestimated. It can been seen that the radius from Equation 5.4 is in the start of the area where the gain estimate stabilises.

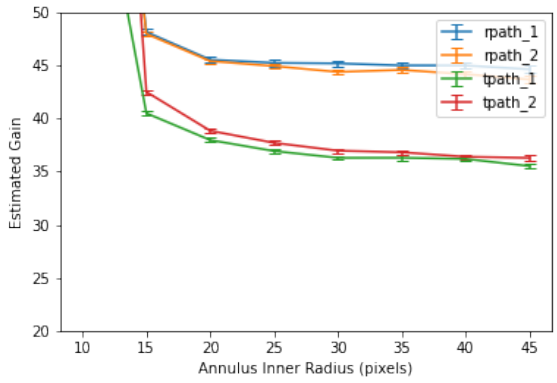

Figure 5.4: The effect of the inner annulus radius of the estimated gain for the four GASP channels. Nominal gain = 200

The other sensitive parameter for this technique is the outer fitting point on the histogram, namely a fraction of the maximum end output value O_f, as mentioned previously. The effect on the gain of varying this parameter may be seen in Figure 5.5(a) along with the line fits for two different values in Figure 5.5(b)(c). In all cases the inner fit point was set at 5σ, where σ is the readnoise standard deviation

In order to see if the estimated gains were consistent across the hundred frames, the frames were subdivided into sets of 10, and the gain calculated for each. The gains remain consistent over the time series, as can be seen in Figure 5.6.

The overall gain results for this method on the standard source data, including the gain ratio, may be seen in Table 5.1

Nominal EM Gain	**RPath 1 EM Gain**	**RPath 2 EM Gain**	**TPath 1 EM Gain**	**TPath 2 EM Gain**	**Gain Ratio**
200	44.88	43.99	36.05	35.65	1.27

Table 5.1: Estimated Gains for GASP channels using Histogram slope method

EMCCD Model Parameters

Using the same data, the EMCCD model parameter methods we used. Using the same set of annular data described above, the resulting PDFs may be found in Figure 5.7. The overall gain results for these methods on the standard source may be seen

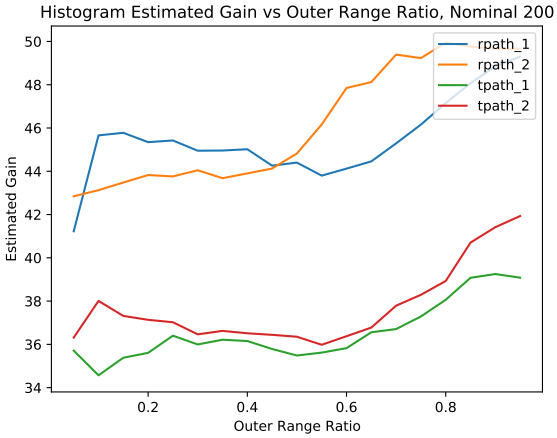

(a)

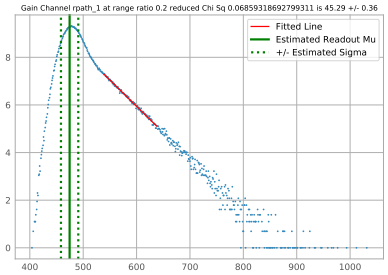

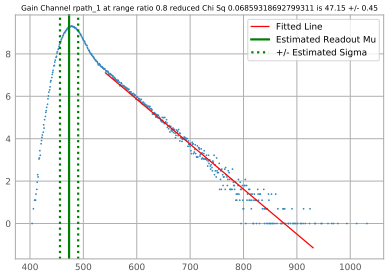

(b) (c)

Figure 5.5: (a) The effect the outer fitting point O_f on the estimated gain for the four GASP channels (b) Line fit for O_f=0.2 (c) Line fit for O_f=0.8

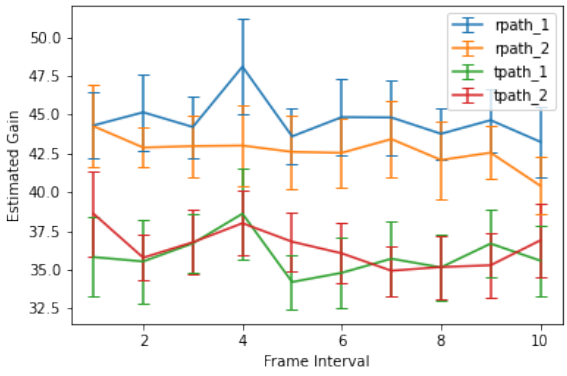

Figure 5.6: The estimated gains over the 100-frame time series, using data from sets of 10 frames

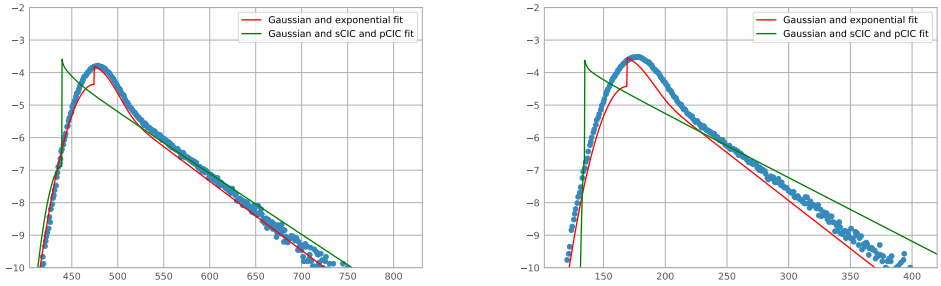

(a) (b)

Figure 5.7: PDF fits for both EMCCD models for (a) RPath and (b) TPath GASP channels

in Table 5.2. It can been seen that the more complex model that accounts for clock induced charge, fails to fit distribution at the relatively low nominal gain level, and overestimates the gain versus the other methods.

Model	**Nominal EM Gain**	**RPath 1 EM Gain**	**RPath 2 EM Gain**	**TPath 1 EM Gain**	**TPath 1 EM Gain**	**Gain Ratio**
Simple Model	200	47.00	46.32	33.87	35.10	1.35
Model w/ CIC	200	53.74	64.24	51.30	45.49	1.21

Table 5.2: Estimated Gains for GASP Channels using EMCCD model fit

COTS

The COTs method (using a 2D Gaussian PDF model for the PSF) was applied to the same data set, producing per-frame estimates. As explained in the theory section, individual frames will generate estimates with high error, but once aggregated over several frames, this error reduces. The results may be seen Figure 5.8(a) in sets of 10 frames. It is apparent that the estimated gains are time-varying, and much higher than those estimated with the previous methods on the same data. In order to understand if this may be underlying variation in the true gain or caused by seeing, an analysis of the seeing condition over time may be seen in 5.8(b), namely the σ of the fitted 2D Gaussian. (The approximate level of seeing as indicated by the FWHM for the sequence is approximately 6 pixels, corresponding to 1.3 arcseconds. This is similar in range to the simulated seeing in Chapter 3, as can be seen in Figure 3.18(c)). It can be seen that there is a strong negative correlation between the sigma (or width of the source), and the estimated gain, which should be largely constant.

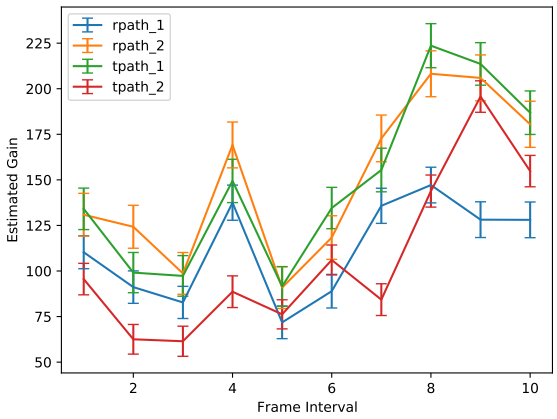

(a)

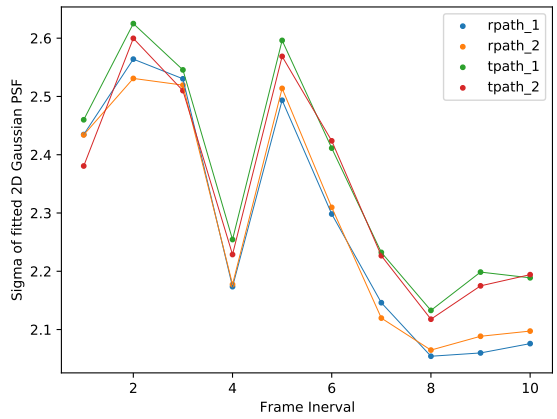

(b)

Figure 5.8: (a) COTs EM Gain estimates for 100 frames (averaged over 10 frame) (b) Sigma of fitted 2D Gaussian PSF

This correlation with the changing sigma appears to indicate that seeing is having a significant effect on the accuracy of this method. In addition, both R-Paths and T-Paths should produce consistent results as they belong to the same detector, but this is not the case. The overall gain estimates for each channel may be found in Table 5.3.

Method	**Nominal EM Gain**	**RPath 1 EM Gain**	**RPath 2 EM Gain**	**TPath 1 EM Gain**	**TPath 1 EM Gain**	**Gain Ratio**
COTs	200	114.3	153.0	150.5	106.2	1.04

Table 5.3: Estimated Gains for Gasp Channels using COTs method

5.4 Crab Nebula results

High speed data was captured from the Crab Nebula, with exposure times for each frame of 0.5 ms. Here the high speed mode of the device, with a very small exposure time, ensures there should be less than one photon of flux per pixel in each frame. The pixel field of data is much smaller in this high-speed configuration, with only an array 13x128 pixels being read out, but with a much larger number of frames (300000). As there is no point spread function to fit, the COTs method cannot be applied to this data. This dataset also has a significantly higher gain than the previous sets, with a nominal EM gain of 1000.

Histogram Slope

A sample histogram from this data set from the RPath channel may be seen in Figure 5.9(a), along with a fitted line. Even without using all the data (10000 frames shown), there is much more data available to produce a robust histogram. The resulting estimated gain using this method is sensitive to both the offset from the bias peak, and the outer range ratio O_f, as can be seen in Figure 5.9(b) and 5.9(d). It can be seen that 5.5 σ is not sufficient starting offset to get out of the non-linear region of the log histogram, with 10 σ being used in the fit shown in 5.9(a). The resulting values for this method may be found in Table 5.4

Method	**Nominal EM Gain**	**RPath 1 EM Gain**	**RPath 2 EM Gain**	**TPath 1 EM Gain**	**TPath 1 EM Gain**	**Gain Ratio**
Histogram Slope	1000	240.44	240.35	216.23	216.44	1.11

Table 5.4: Estimated Gains for Gasp Channels using Histogram slope method

EMCCD Model Parameters

The EMCCD parameter modelling techniques to estimate EM gain were applied, and the results are shown in Figure 5.10 and table 5.5.

Method	**Nominal EM Gain**	**RPath 1 EM Gain**	**RPath 2 EM Gain**	**TPath 1 EM Gain**	**TPath 1 EM Gain**	**Gain Ratio**
Simple Noise Model	1000	241.00	241.12	223.55	224.53	1.075
Noise Model w/ CIC	1000	240.77	246.70	225.47	224.92	1.08

Table 5.5: Estimated Gains for Gasp Channels using EMCCD model parameters method

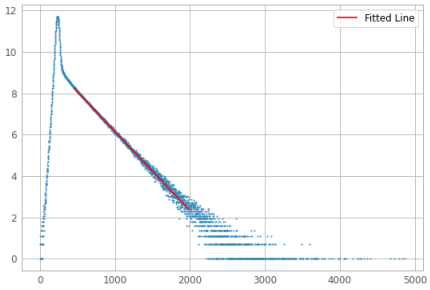

(a)

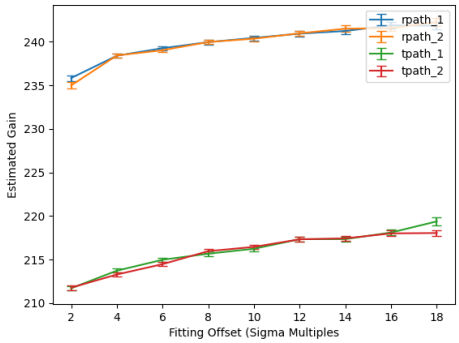

(b)

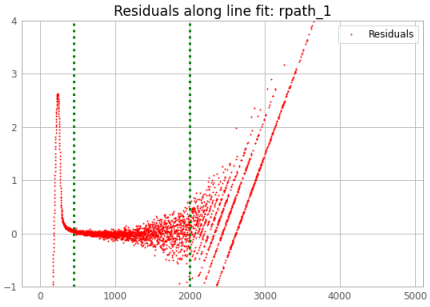

(c)

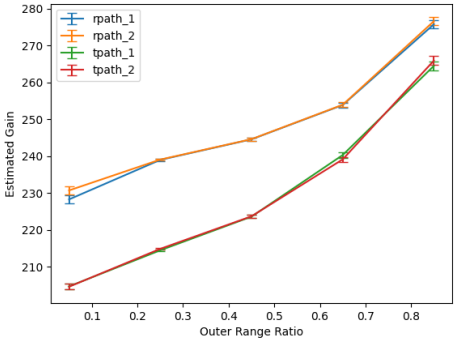

(d)

Figure 5.9: (a) Output log histogram of rpath 1 channel and fitted line in red. Fitting point sets at 10 σ offset and $O_f = 0.35$ (c) The residuals along the line fit (b) Sensitivity of estimated gain to the offset in estimated noise sigma from the output bias (d) Sensitivity of estimated gain to the outer range ratio O_f

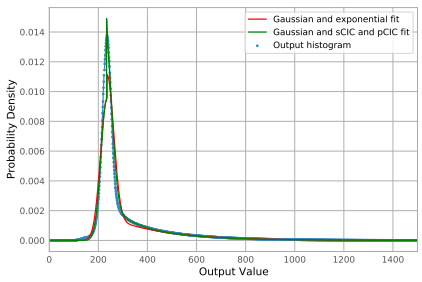

(a)

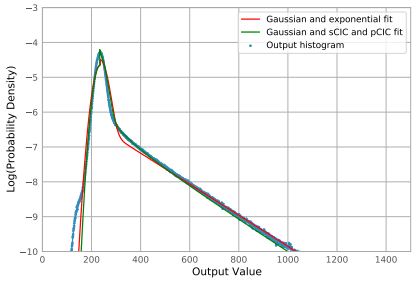

(b)

Figure 5.10: (a) Output histogram for TPath Channel with the PDFs for each model shown (b) The same but with the log histogram.

Implication of gain error on GASP polarisation measurements

While the estimation of polarisation parameters from the GASP instrument is not dependant on the individual estimate gains, it is dependant on the ratio between the estimated gain for each channel, as detailed in Equation 5.1. Further details on the relationship between this ratio and polarisation estimates may be found in O'Connor [15]. For the same NGC 08169-00417 standard source data used in this chapter, an analysis of the relationship between the estimated gain ratio and the Linear Polarisation may be found in Figure 5.11, which is taken from Shearer [in preparation]. In this case the histogram slope method was used.

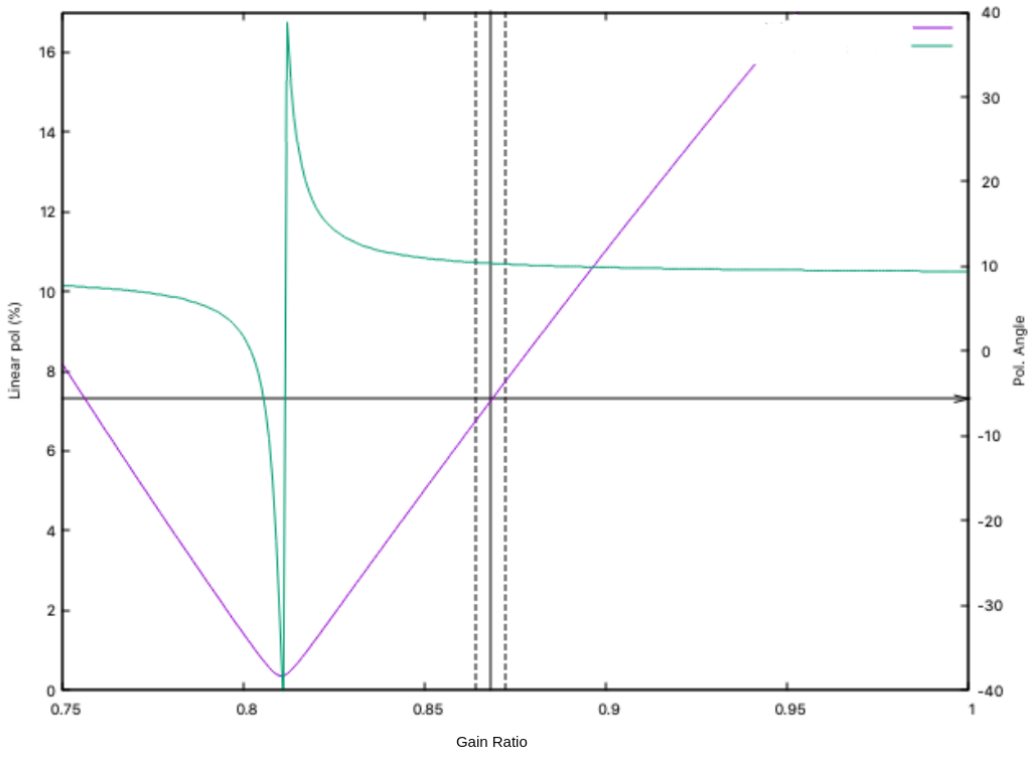

(a)

Figure 5.11: Relationship between the Polarisation estimates from from GASP and the gain ratio estimates. Purple is the linear polarisation and turquoise is the polarisation angle. The standard error of the gain ratio is show by the dashed lines. The horizontal line represents the previously estimated linear polarisation of this standard. Gain ratio is inverted versus ratio estimated in text.

Summary of Astronomical results

Comparing the histogram slope method to the EMCCD noise model methods, it can be seen that the results are very consistent at high gain levels (high speed Crab Data), but for data with lower gain (low speed Standard Sources), the more complex noise model with the clock induced charge model fails to fit the histogram and produces inconsistent results. One advantage with using the noise model methods is that they require less tuning of the start and end fitting points, which were observed to have a big impact on the accuracy of the results when fitting a line to the histogram. While there was variation in the seeing during the image sequence, these methods appeared to be unaffected by the seeing level provided the annulus was chosen to adapt to the seeing level.

The COTS method did not produce results consistent with the other methods for the low speed standard source data. This was clear in both the absolute estimated gain values, but also in the time varying estimates that were not seen in the other methods. It is possible that due to the short exposure time, there was not enough integration to produce a stable seeing disc upon which the method rests. As longer integrated data from the instrument was not available, whether longer integration could make this a viable method for application to astronomy remains an open question. What was clear is that the variation in estimated gains across across the sequence of images was correlated with the seeing conditions.

Similar to the lab results, the estimated EM gain values for all methods for both types of astronomical data was significantly lower than the nominal values set on the detector, at approximately a quarter the nominal value. As mentioned in the previous chapter, provided this is difference is linear across different gain values, it should not be a problem for the accuracy of the relative gains between the two detectors, which is what is needed for the GASP instruments polarimetry calculations.

Chapter 6

Discussion and Conclusions

A variety of techniques to estimate the multiplicative gain in EMCCDs were researched and experimented in this work including several new techniques developed in fields outside of Astronomy, to investigate their potential use.

The histogram slope technique, while the most commonly used in astronomical settings (and previously the standard technique for gain calibration of the GASP instrument), was found to be sensitive to a number of parameters, including the area of the source image used (i.e. inner annulus radius), and the start and end fitting points. Techniques to formalize the selection of these parameters were explored and tested.

The EMCCD noise model approaches were shown to work better at higher gains, and have the advantage of having to configure less parameters during their use. The more complex model showed potentially less bias in the face of higher clock induced charge in simulation, but produced similar results on the high gain astronomical data to the simpler model. It was also noted that higher gain levels are also required for these model methods to start fitting correctly.

The Calibration-On-The-Spot technique was applied to the astronomical domain from microscopy, and has numerous advantages if it could be made work. While through simulation, it appeared the method could work for astronomical sources in the presence of seeing effects, if there was sufficient integration, it failed to produce consistent results on the data from the GASP instrument. It could be explored in the future after capturing longer exposures of sources if it could be viable alternative in some scenarios for gain calibration.

More traditional techniques for estimating the gain of EMCCDs, namely the mean variance techniques have been used in laboratory environments, when it is possible to collect a more detailed set of intensity series calibration points. These were tested in the laboratory alongside a new gain series methods, where the input intensity levels do not need to be varied, which was found to produce the similar results. The latter might be more practical to implement at a telescope where different intensity levels might not be possible.

All the techniques applied in the lab and on real data, showed a large discrepancy from the manufacturers nominal gain, between 2x and 4x less. It is not clear what the cause of this discrepancy is or if this is normal for the particular devices used. Another possibility is that the detectors used may have aged.

The ability to explore the effect of seeing in a simulation environment was explored, and a full end to end simulation flow was built. As part of this, the AOTools package was also analyzed, to the see if it produced outputs in line with the Komologorov theory, which it was found to. Also a software library to simulate essentially an unlimited amount of photo-electrons through and EMCCD register processes was developed, which may be of use to future researchers in this area.

Bibliography

[1] Boyle W. S. Smith G. E. “Charge Coupled Semiconductor Devices”. In: *Bell System Technical Journal* 49 (1970), p. 587 593. URL: https://doi.org/10.1117/3.374903https://doi.org/10.1002/j.1538-7305.1970.tb01790.x.

[2] James Janesick. “Scientific Charge-Coupled Devices”. In: *SPIE* (2001). URL: https://doi.org/10.1117/3.374903.

[3] Ian S. McLean. “Electronic Imaging in Astronomy”. In: *Springer Praxis Books* (Aug. 2008). DOI: /10.1007/978-3-540-76583-7. URL: https://doi.org/10.1007/978-3-540-76583-7.

[4] Paul Jerram et al. “The LLCCD: low-light imaging without the need for an intensifier”. In: *SPIE Proceedings* 4306 (May 15, 2001), pp. 178–186. DOI: 10.1117/12.426953. URL: https://lens.org/123-096-822-904-121.

[5] Craig D. Mackay et al. “Subelectron read noise at MHz pixel rates”. In: *SPIE Proceedings* 4306 (May 15, 2001), pp. 289–298. DOI: 10.1117/12.426988. URL: https://lens.org/137-498-009-655-978.

[6] S. M. Tulloch, P. Rodrı guez-Gil, and V. S. Dhillon. “Radial velocity study of the post-period minimum cataclysmic variable SDSS J143317.78101123.3 with an electron-multiplying CCD”. In: *Monthly Notices of the Royal Astronomical Society: Letters* 397.1 (July 2009), pp. L82–L86. DOI: 10.1111/j.1745-3933.2009.00689.x. URL: https://doi.org/10.1111%2Fj.1745-3933.2009.00689.x.

[7] V. S. Dhillon et al. “ULTRASPEC: High-speed spectroscopy with zero readout noise”. In: *AIP Conference Proceedings* 984.1 (Feb. 2008), pp. 132–139. ISSN: 0094-243X. DOI: 10.1063/1.2896922. eprint: https://pubs.aip.org/aip/acp/article-pdf/984/1/132/11881504/132_1_online.pdf. URL: https://doi.org/10.1063/1.2896922.

[8] A. G. Basden, C. A. Haniff, and C. D. Mackay. “Photon counting strategies with low-light-level CCDs”. In: *Monthly Notices of the Royal Astronomical Society* 345.3 (Nov. 2003), pp. 985–991. ISSN: 0035-8711. DOI: 10.1046/j.1365-8711.2003.07020.x. URL: https://doi.org/10.1046/j.1365-8711.2003.07020.x.

[9] Harpsøe, K. B. W. et al. “High frame rate imaging based photometry - Photometric reduction of data from electron-multiplying charge coupled devices (EMCCDs)”. In: *A&A* 542 (2012), A23. DOI: 10.1051/0004-6361/201219059. URL: https://doi.org/10.1051/0004-6361/201219059.

[10] Harpsøe, K. B. W., Andersen, M. I., and Kjægaard, P. "Bayesian photon counting with electron-multiplying charge coupled devices (EMCCDs)". In: *A&A* 537 (2012), A50. DOI: 10.1051/0004-6361/201117089. URL: https://doi.org/10.1051/0004-6361/201117089.

[11] Hirsch M et al. "A Stochastic Model for Electron Multiplication Charge-Coupled Devices – From Theory to Practice". In: *PLoS ONE* 8 (2013). DOI: 10.1371/journal.pone.0053671. URL: https://www.doi.org/10.1046/j.1365-8711.2003.07020.x.

[12] Robert N. Tubbs. "Lucky Exposures: Diffraction limited astronomical imaging through the atmosphere". In: *arXiv* (2003). DOI: 10.48550/ARXIV.ASTRO-PH/0311481. URL: https://arxiv.org/abs/astro-ph/0311481.

[13] S. M. Tulloch and V. S. Dhillon. "On the use of electron-multiplying CCDs for astronomical spectroscopy". In: *Monthly Notices of the Royal Astronomical Society* 411.1 (Jan. 2011), pp. 211–225. ISSN: 0035-8711. DOI: 10.1111/j.1365-2966.2010.17675.x. URL: https://doi.org/10.1111/j.1365-2966.2010.17675.x.

[14] Duncan P. Ryan et al. "A gain series method for accurate EMCCD calibration". In: *Scientific Reports* 11 (Sept. 2021). ISSN: 2045-2322. DOI: 10.1038/s41598-021-97759-6. URL: https://doi.org/10.1038/s41598-021-97759-6.

[15] Eoin O'Connor. "Development of a high time resolution optical polarimeter for astronomy". In: *PhD Theses, University of Galway* (Dec. 2018). URL: http://hdl.handle.net/10379/14897.

[16] Kim I. Mortensen and Henrik Flyvbjerg. ""Calibration-on-the-spot": How to calibrate an EMCCD camera from its images". In: *Scientific Reports* 6.1 (July 2016). DOI: 10.1038/srep28680. URL: https://doi.org/10.1038/srep28680.

[17] A. F. J. Moffat. "A Theoretical Investigation of Focal Stellar Images in the Photographic Emulsion and Application to Photographic Photometry". In: *Astronomy & Astrophysics* 3 (1969), pp. 455–461.

[18] Thomas P. Robitaille et al. "Astropy: A community Python package for astronomy". In: *Astronomy &amp Astrophysics* 558 (Sept. 2013), A33. DOI: 10.1051/0004-6361/201322068. URL: https://doi.org/10.1051%2F0004-6361%2F201322068.

[19] M. J. Townson et al. "AOtools: a Python package for adaptive optics modelling and analysis". In: *Optics Express* 27.22 (Oct. 2019), p. 31316. ISSN: 1094-4087. DOI: 10.1364/oe.27.031316. URL: http://dx.doi.org/10.1364/OE.27.031316.

[20] Olivier Daigle, Claude Carignan, and Sébastien Blais-Ouellette. "Faint flux performance of an EMCCD". In: *High Energy, Optical, and Infrared Detectors for Astronomy II* (June 2006). Ed. by David A. Dorn and Andrew D.Editors Holland. DOI: 10.1117/12.669433. URL: http://dx.doi.org/10.1117/12.669433.

[21] e2v technologies. "Low Light Technical Note 5 An Overview of the Ageing Characteristics of L3Vision TM Sensors". In: *e2v technologies* (Aug. 2017). URL: https://www.teledyne-e2v.com/content/uploads/2017/08/low-light_TN5.pdf.

[22] Andreas Quirrenbach. "The effects of atmospheric turbulence on astronomical observations". In: *A. Extrasolar planets. Saas-Fee Advanced Course* 31.137 (2006), p. 137.

[23] Robert J. Noll. "Zernike polynomials and atmospheric turbulence∗". In: *J. Opt. Soc. Am.* 66.3 (Mar. 1976), pp. 207–211. DOI: 10.1364/JOSA.66.000207. URL: https://opg.optica.org/abstract.cfm?URI=josa-66-3-207.

[24] Mette Owner-Petersen and Alexander V. Goncharov. "Some consequences of atmospheric dispersion for ELTs". In: *Ground-based Telescopes* 5489 (2004), pp. 507–517. DOI: 10.1117/12.551371. URL: https://doi.org/10.1117/12.551371.

[25] Duncan P Ryan. "EMCCD Calibration Library". In: *github* (Last accessed 2022). URL: https://github.com/ryand-LANL/EMCCD-calibration.

Appendix A

Source Code

Several libraries were developed during the course of this work, and they have been made available in public github repositories. In addition to the code, examples of use and tests are provided where relevant.

A.1 Photon Generator

Library to generator synthetic input data of sources described in the simulation chapter:

`https://github.com/fatmac78/photon_generator`

A.2 EMCCD simulator

Library to simulate the EMCCD detector, including the multiplicative process in the serial register, clock induced charge in the serial register, and output bias and readout noise

`https://github.com/fatmac78/emccd_simulator`

A.3 Calibration-on-the-Spot Estimator

Library to estimate the EMCCD parameters using the Calibration-on-the-spot technique. Modified version of code supplementary to Mortensen [16]

`https://github.com/fatmac78/calibration_on_the_spot`

A.4 EMCCD Mixture Model Estimator

Library that was used to estimate EMCCD parameters using mixture model deailed in equation 1.13

`https://github.com/fatmac78/emccd-mixture-model`

A.5 Guassian Exponential Mixture Model Estimator

Library to estimate EMCCD parameters using simple Gaussian and Exponential mixture details in equation 1.8

`https://github.com/fatmac78/gaussian-exponential-mixture`